

# Amphibole-rich cumulate xenoliths in the Zhazhalong intrusive suite, Gangdese arc: Implications for the role of amphibole fractionation during magma evolution

JIN-SHENG ZHOU<sup>1,2,\*</sup>, ZHU-SEN YANG<sup>3</sup>, ZENG-QIAN HOU<sup>1</sup>, AND QIANG WANG<sup>2,4,5</sup>

<sup>1</sup>Institute of Geology, Chinese Academy of Geological Sciences, Beijing 100037, China

<sup>2</sup>State Key Laboratory of Isotope Geochemistry, Guangzhou Institute of Geochemistry, Chinese Academy of Sciences, Guangzhou 510640, China

<sup>3</sup>MLR Key Laboratory of Metallogeny and Mineral Assessment, Institute of Mineral Resources, CAGS, Beijing 100037, China

<sup>4</sup>CAS Center for Excellence in Tibetan Plateau Earth Sciences, Beijing 100101, China

<sup>5</sup>College of Earth and Planetary Sciences, University of Chinese Academy of Sciences, Beijing 10049, China

## ABSTRACT

Amphibole fractionation during the early evolution of arc magmas has been widely inferred on the basis of distinctive geochemical fingerprints of the evolved melts, although amphibole is rarely found as a major mineral phase in arc volcanic rocks, so-called cryptic amphibole fractionation. Here, we present a detailed case study of xenoliths of amphibole-rich cumulate from the Zhazhalong intrusive suite, Gangdese arc, which enables an investigation of this differentiation process using a combination of petrological observations and in situ geochemical constraints. Evidence that the xenoliths represent fragments of igneous cumulates includes: (1) the presence of an amphibole-dominated crystal framework; (2) mineral and whole-rock Fe–Mg exchange coefficients; (3) rare-earth element patterns that are similar in the amphiboles and the xenoliths; (4) the compositions of basaltic to andesitic liquids in equilibrium with amphiboles; and (5) enrichment of the xenoliths in compatible elements and depletion in incompatible elements. The amount of trapped liquid based on La, Ce, and Dy abundances varies from ~12 to ~20%. Actinolitic cores within amphibole grains likely represent reaction between olivine precursor and hydrous melt, as evidenced by their high Cr and Ni contents. Amphibole thermometry and oxybarometry calculations indicate that crystal accumulation occurred over temperatures of 857–1014 °C, at mid-crustal pressures of 312 to 692 MPa and oxygen fugacity between 0.4 and 1.9 log units above the nickel–nickel oxide buffer. Quantification of the major-element compositions of the parent liquids indicates that the Zhazhalong amphibole cumulates crystallized from basaltic to andesitic magmas, probably with a shoshonitic affinity, and with SiO<sub>2</sub> contents of 46.4–66.4 wt%. Appropriate partition coefficients, calculated using a parameterized lattice strain model and an empirical partitioning scheme, were employed to calculate the trace-element compositions of the liquids in equilibrium with amphibole. Our results confirm that Dy/Yb and Dy/Dy\* ratios, which decrease with increasing degrees of differentiation, can be used as robust signatures of amphibole fractionation. This work presents a direct snapshot of the process of amphibole fractionation and provides a natural example of the hidden amphibole “sponge” in arc crust. In particular, this study also suggests that some appinites likely represent amphibole-rich cumulates, which may help to explain the genesis of other unusual but petrologically significant rocks.

**Keywords:** Amphibole, fractional crystallization, cumulate, magma evolution, trace element

## INTRODUCTION

Arc magmatism at subduction zones represents the sites of production of new continental crust (Rudnick 1995). There is a little dispute that primitive arc magmas are generated by partial melting in the mantle wedge in response to the dehydration of down-going slabs (e.g., Tatsumi 1989; Hawkesworth et al. 1993; Ulmer and Trommsdorff 1995; Grove et al. 2002). However, few of these mantle-derived magmas reach the surface without significant modification. Various processes have been proposed to explain the origin of evolved magmas. Remelting of the preexisting crust is commonly invoked in the petrogenesis of granitoid plutons (e.g., Chappell and White 1992; Clemens and Stevens 2012; Brown 2013), and there is compelling evidence for a genetic

link between metasedimentary rocks and strongly peraluminous granites (Chappell and White 1992). Crustal melting is efficient where heat is supplied by underplating mafic magmas (e.g., Petford et al. 2000). Thus, partial melting of the crust is sometimes regarded as a concomitant process in deep-crustal hot zones, where fractional crystallization of mantle-derived basaltic parents, partial melting of the surrounding crust, and hybridization of residual and crustal melts occur simultaneously (Hildreth and Moorbath 1988; Annen et al. 2006).

Over the past decade, a growing number of studies have supported fractional crystallization of hydrous basaltic magmas as the dominant process responsible for the production of intermediate and silicic magmas (e.g., Lee and Bachmann 2014; Jagoutz and Klein 2018). Experimental results suggest that the origin of compositional diversity in magmas can be attributed mainly to fractional crystallization (e.g., Grove and Brown 2018; Müntener and Ulmer 2018). Field observations and detailed studies of natural rock

\* Present address: State Key Laboratory of Isotope Geochemistry, Guangzhou Institute of Geochemistry, Chinese Academy of Sciences, Guangzhou 510640, China. E-mail: jinshengzhou@gig.ac.cn

suites, such as the well-exposed Kohistan Arc Complex, Pakistan, support the laboratory data (e.g., Jagoutz et al. 2006). Recently, an emerging view has been that magmas within transcrustal magmatic systems are stored as high-crystallinity mushes (e.g., Bachmann and Huber 2016; Cashman et al. 2017), providing a potential physical mechanism for fractional crystallization in crustal distillation columns (e.g., Bachmann and Huber 2019). However, this concept is debated, in particular with respect to explaining the relationship between volcanic and plutonic rocks (e.g., Bachmann et al. 2007; Glazner et al. 2015), and the genesis of zoned intrusive suites (e.g., Clemens and Stevens 2012; Coleman et al. 2012; Putirka et al. 2014; Barnes et al. 2016).

Research has become increasingly focused on the detailed processes of fractional crystallization during magma evolution. Most arc magmas are enriched in H<sub>2</sub>O (Plank et al. 2013) and can stabilize amphibole at pressures corresponding to the middle and lower crust (e.g., Grove et al. 2003; Alonso-Perez et al. 2009). Although amphibole is rarely present as a major mineral in erupted volcanic rocks (Davidson et al. 2007), probably owing to the instability of amphibole at low pressures (Rutherford and Devine 1988), trends of increasing La/Yb and decreasing Dy/Yb with increasing SiO<sub>2</sub> suggest that removal of amphibole is widespread during the evolution of arc magmas (so-called “cryptic amphibole fractionation”; Davidson et al. 2007). If so, this amphibole “sponge” would accumulate at intermediate crustal depths and may constitute a significant reservoir of H<sub>2</sub>O (Davidson et al. 2007). Thus, determining where these hidden amphibole sponges are located, how they form, and how they affect magma differentiation is critical to better understanding crustal growth and the crustal water reservoir. Studies of derivative magmas may fail to provide convincing evidence concerning this differentiation process, because liquids derived from different processes may have similar chemical compositions (e.g., Müntener and Ulmer 2018). In contrast, crustal cumulates may be more useful in constraining deep magmatic processes (e.g., Chin et al. 2018). Hence, there has been increasing interest in the use of amphibole-rich xenoliths to explore the formation of amphibole-rich cumulates and the role of amphibole fractionation during magma evolution (e.g., Tiepolo and Tribuzio 2008; Tollan et al. 2012; Smith 2014; Stamper et al. 2014; Cooper et al. 2016; Klaver et al. 2017; Melekhova et al. 2017; Chang and Audétat 2018).

Exposed within the Himalayan–Tibetan orogen, the Gangdese arc is an ideal place to assess amphibole fractionation and its influences on the evolution of arc magmas because it includes abundant amphibole-rich mafic intrusions and xenoliths (e.g., Ma et al. 2013; Xu et al. 2015; Meng et al. 2016; X. Ma et al. 2018; Wang et al. 2019; Xu et al. 2019). We performed a detailed case study of amphibole-rich xenoliths within the Zhazhalong intrusive suite, part of the Gangdese arc. Whole-rock and mineral chemistry were carried out on the xenoliths to explore their petrogenesis and to provide a quantitative assessment of the role of amphibole fractionation during magma evolution.

## GEOLOGIC SETTING

The Gangdese arc, exposed in the large-scale Himalayan–Tibetan orogen, is a fossil continental arc that was sandwiched between the Indian and Asian plates during continental collision and that extends along strike for more than 1500 km (Chung et al. 2005).

To the northwest, the arc connects with the Ladakh and Kohistan arcs (Fig. 1; Ji et al. 2009; Jagoutz 2010). The Gangdese arc is subdivided into northern and southern parts, which are bounded by the Luobadui–Milashan Fault. The northern part is located within the central Lhasa subterrane, where most igneous rocks have highly evolved isotopic compositions, whereas the southern part extends along the Eurasian continental margin, where most of the magmatic rocks have less radiogenic isotopic compositions (e.g., Zhu et al. 2011; Hou et al. 2015a). Although the precise time of initial collision between the Indian and Asian continents remains controversial (Ding et al. 2017), Triassic to early Tertiary magmatism in the Gangdese arc originated through subduction of the Tethyan Ocean lithosphere along the southern margin of the Lhasa Terrane (Chung et al. 2005). A minimum age for initiation of subduction is indicated by ~237 Ma andesites, although the polarity of subduction is debated (e.g., Ji et al. 2009; Zhu et al. 2011). Zircon U–Pb ages show that magmatic activity in the arc occurred between 237 and 10 Ma (e.g., Ji et al. 2009; Zhu et al. 2011; Hou et al. 2015a), with this magmatism being represented mainly by the voluminous Gangdese Batholith and coeval volcanic rocks. The magmatism can be divided into four stages, with corresponding peaks of ~190, ~90, ~50, and ~16 Ma (Zhu et al. 2011; Ji et al. 2014). The most voluminous and intense magmatic event occurred during the early Tertiary (~50 Ma) (Mo et al. 2008). The Gangdese Batholith comprises gabbro, diorite, granodiorite, monzogranite, and syenogranite (e.g., Ji et al. 2009), along with peraluminous leucogranites (e.g., L. Ma et al. 2018). Amphibole-rich intrusions and xenoliths are associated primarily with intrusions that pre-date the India–Eurasia collision (e.g., Ma et al. 2013; Xu et al. 2015; Ma, X. et al. 2018; Wang et al. 2019; Xu et al. 2019).

## SAMPLING AND PETROLOGY

The xenoliths studied here were collected from granites of the Zhazhalong intrusive suite, which is located in the central Gangdese arc (Fig. 1). In hand specimen, the xenoliths are black or dark–brown in color (Supplemental<sup>1</sup> Fig. S1) and contain abundant amphibole with grain sizes generally between 0.1 and 1 mm (Figs. 2a and 2b). Amphibole crystals are euhedral or subhedral and commonly display a poikilitic texture, with large oikocrysts containing euhedral to subhedral crystals of Cr-spinel, minor apatite (Fig. 2c), and pyrite. Magnetite rims around Cr-spinel grains are common (Fig. 2c). The groundmass is generally dominated by irregularly shaped quartz and K-feldspar, with minor plagioclase. K-feldspar shows extensive low-temperature alteration. Acicular grains of apatite are also present.

The crystallization sequence of the xenoliths can be determined through textural observations. Cr-spinel was the first phase to crystallize, followed by amphibole. Apatite occurs as inclusions in amphibole as well as acicular crystals in the groundmass, suggesting a wide range of crystallization interval. Fine-grained anhedral quartz and K-feldspar in the groundmass likely crystallized from the interstitial liquid. In addition, some amphibole grains have cores of actinolite (Fig. 2d).

## ANALYTICAL METHODS

Zircon U–Pb dating of the host granites was performed using a Neptune multi-collector inductively coupled plasma–mass spectrometry (ICP–MS) instrument coupled with a Newwave UP213 laser-ablation (LA) system at the Institute of Mineral Resources, Chinese Academy of Geological Sciences, Beijing, China. The operating

conditions used during the analyses were a beam diameter of 25  $\mu\text{m}$ , a repetition rate of 10 Hz, and a beam energy of 2.5 J/cm<sup>2</sup>. Analyses used the GJ-1 zircon as an internal standard. Detailed operating conditions and analytical procedures followed Hou et al. (2009). Off-line selection, integration of background and analytical signals, time-drift corrections, and quantitative calibrations for the U–Pb data were calculated using the software *ICPMSDataCal* (Liu et al. 2010).

Major- and trace-element analyses were performed at the Analytical Laboratory of the Beijing Research Institute of Uranium Geology, Beijing, China. Major-element compositions were determined using X-ray fluorescence spectrometry for which the analytical uncertainty was better than 1%. Trace-element analyses were performed using ICP–MS for which the precision was better than 5%.

Compositions of minerals within the xenoliths were analyzed using a JEOL JXA 8230 electron probe micro-analyzer with a 15 kV accelerating voltage, 20 nA beam current, and 1  $\mu\text{m}$  spot size, at the Key Laboratory of Mineralogy and Metallogeny of the Guangzhou Institute of Geochemistry, Chinese Academy of Sciences (GIG–CAS), Guangzhou, China, and a JEOL JXA 8100 electron microprobe (EMP) with a 15 kV accelerating voltage, 20 nA beam current, and 5  $\mu\text{m}$  spot size, at the Institute of Geology, Chinese Academy of Geological Sciences, Beijing, China. In both cases, ZAF correction routines were employed, and both natural and synthetic standards were used. Trace-element abundances were measured by an ELEMENT XR (Thermo-Fisher Scientific) ICP–sector field (SF)–MS instrument coupled with a 193 nm (ArF) Resonetics RESOLUTION M-50 LA system at the State Key Laboratory of Isotope Geochemistry (SKLlABIG), at GIG–CAS. All LA–ICP–MS spots were located over EMPA spots. Analyses used a spot size of 33  $\mu\text{m}$ , a laser repetition rate of 5 Hz, and a pulse energy of ~4 J/cm<sup>2</sup>. A smoothing device (The Squid, Laurin Technic) was used to smooth the sample signal. For each analysis, a 20 s gas blank (laser off) and a 30 s sample signal (laser on) were collected and recorded. Measurements were carried out under the E-scan mode. U.S. Geological Survey (USGS) reference glasses BHVO-2G, BCR-2G, and GSD-1G were employed to construct the calibration line for each element. The oxide molecular yield (<sup>238</sup>U/<sup>238</sup>U ratio) was less than 0.3%. USGS reference glass TB-1G was determined as an unknown sample, which indicated that most elements are within 10% of the reference values, with an analytical precision (2RSD, relative standard deviations) of better than 12% for most elements (Supplemental Table S1). Details of the experimental procedure and data reduction strategy used are described by Zhang et al. (2019). SiO<sub>2</sub> contents determined by electron microprobe were used as an internal standardization to normalize trace-element abundances.

## RESULTS

### Zircon U–Pb geochronology

LA–ICP–MS U–Pb dating was performed on euhedral and complexly zoned zircons from two host granites, with a total of 50 analyses being obtained. The data and concordia diagrams are given in Supplemental Table S2 and presented in Supplemental Figure S1, respectively. One sample yielded a weighted mean age of 209.7  $\pm$  2.6 Ma (2 $\sigma$ ;  $n$  = 15; MSWD = 0.3), and another yielded an age of 208.4  $\pm$  1.8 Ma (2 $\sigma$ ;  $n$  = 17; MSWD = 1.6). Although we did not find an appropriate method to determine the age of the xenoliths, cross-cutting granitic veins (Supplemental Fig. S2) indicate that the xenoliths formed before solidification of the host granite, during the early stages of Neotethyan subduction (Ji et al. 2009).

### Whole-rock geochemical compositions

Whole-rock chemical compositions of the Zhazhalong xenoliths and host granites are presented in Table 1. The xenoliths have SiO<sub>2</sub> contents varying from 42.41 to 45.95 wt%, with Al<sub>2</sub>O<sub>3</sub> abundances from 13.00 to 13.97 wt%, Fe<sub>2</sub>O<sub>3</sub> (total) abundances from 9.40 to 10.46 wt%, MgO contents from 9.58 to 11.37 wt%, CaO abundances from 7.52 to 11.90 wt%, and K<sub>2</sub>O abundances from 1.75 to 3.86 wt%. The Mg# (atomic Mg/[Mg + Fe<sub>total</sub>]  $\times$  100) ranges from 67 to 69. On chondrite-normalized rare-earth element (REE) plots (Fig. 3), the xenoliths are depleted in heavy REEs (HREEs), enriched in light REEs (LREEs), and have weak negative Eu anomalies. They have near-chondritic or slightly sub-chondritic Zr/Hf ratios (30.2 to 35.8), sub-chondritic Nb/Ta ratios (10.9 to 15.7),

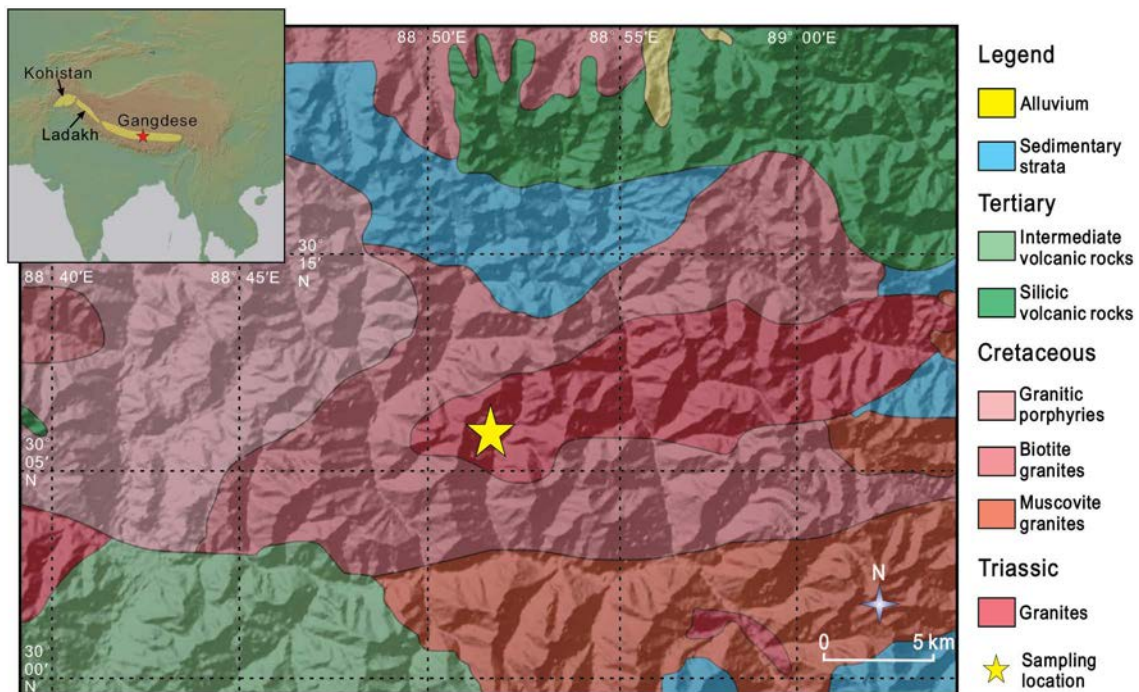


**FIGURE 1.** Geologic map of the Zhazhalong intrusive suite showing the sampling location of the amphibole-rich xenoliths. The inset map shows the location of the Gangdese arc and the neighboring Ladakh and Kohistan arcs. The red star in the inset map marks the location of the study area. (Color online.)

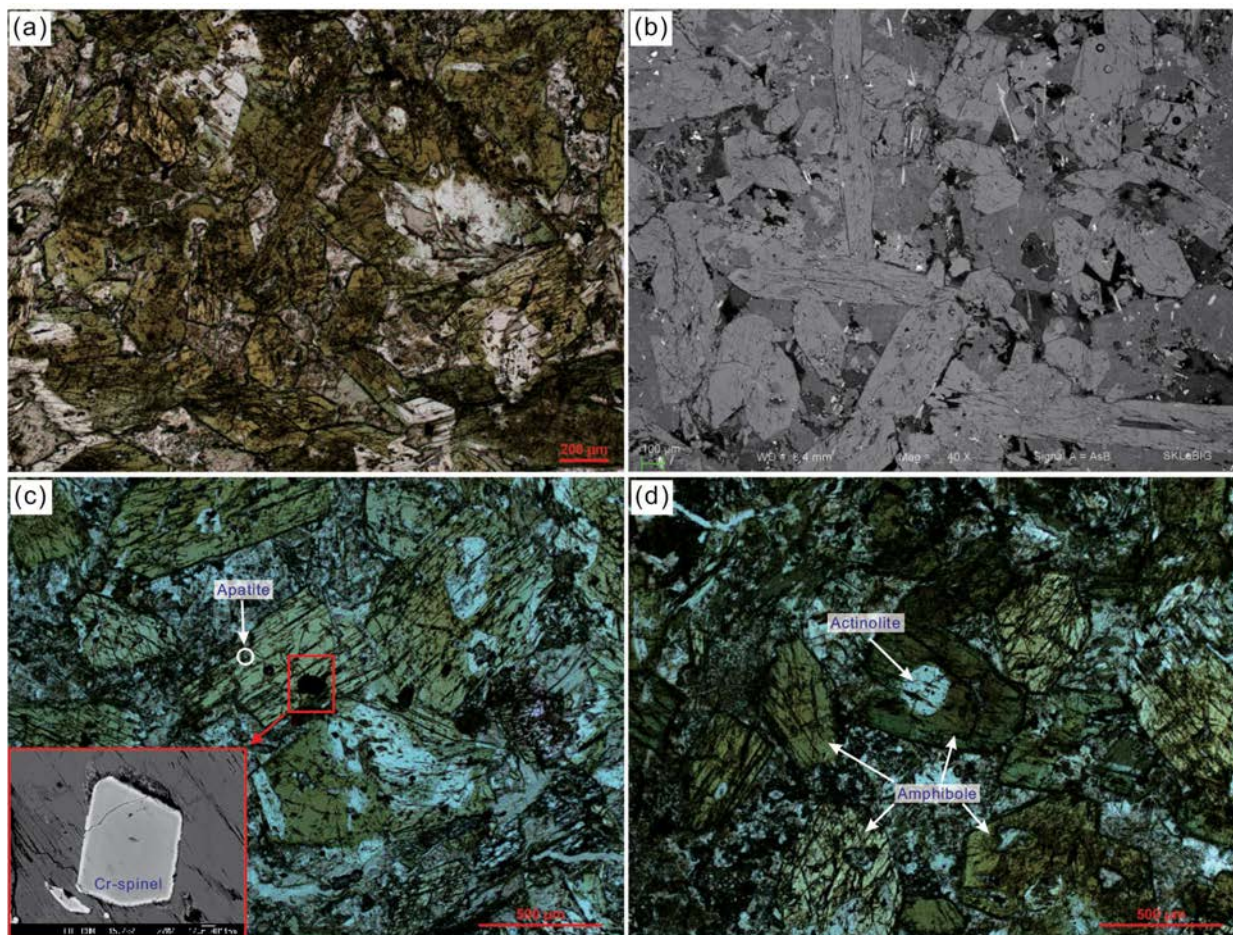


**FIGURE 2.** Photomicrographs of the xenoliths. (a–b) Framework composed of idiomorphic amphibole, anhedral K-feldspar, quartz, and plagioclase. (c) Poikilitic amphibole crystal containing a large oikocryst of euhedral Cr-spinel. (d) Actinolitic core within calcic amphibole. (a, c, and d) are in plane-polarized light; (b) and the inset image in c are backscattered electron microscopy (BSE) images. (Color online.)

Sr/Y ratios (13.0 to 15.9), high Dy/Yb values (1.9 to 2.6), and low Dy/Dy\* values (0.5 to 0.6), where  $Dy/Dy^* = Dy_N / (La_N^{4/13} \times Yb_N^{9/13})$  (Davidson et al. 2013), and  $Dy_N$ ,  $La_N$ , and  $Yb_N$  represent chondrite-normalized (Sun and McDonough 1989) values of Dy, La, and Yb, respectively.

#### Mineral major- and trace-element compositions

Representative analyses for the major- and trace-element contents of different minerals are given in Tables 2–4; the full list of analyses of amphibole is provided in Supplemental Table S1.

#### Amphibole

Magmatic amphibole in the xenoliths displays a narrow range in  $SiO_2$  (37.92–43.58 wt%) and  $Al_2O_3$  (10.55–14.49 wt%) contents. It is characterized by a limited range in Ti (0.06 to 0.37 atoms per formula unit, apfu; per 23 oxygen),  $Al_{total}$  (1.49 to 2.57 apfu), and alkali (Na+K; from 0.34 to 0.92 apfu) contents, and has Mg# of 62–74. Most of the amphiboles are classified as magnesiohastingsite or pargasite (Leake et al. 1997; Fig. 4). Hereafter, we use the term “amphibole” when referring to

magnesiohastingsite or pargasite. On chondrite-normalized REE diagrams (Fig. 3), the amphiboles are enriched in LREEs, depleted in HREEs, and have weak or absent Eu anomalies. Amphibole compositions have a range of Zr/Hf (22.1 to 42.1), Nb/Ta (16.1 to 26.0), Sr/Y (12.0 to 20.6), Dy/Yb (1.7 to 3.0), and Dy/Dy\* (0.4 to 0.9) ratios.

#### Actinolite

Actinolite commonly occurs as inclusions in amphibole (Fig. 2d). Compared with the composition of amphibole, actinolite contains higher  $SiO_2$  (54.22–56.01 wt%) and MgO (19.55–20.76 wt%) contents, and lower  $Al_2O_3$  (0.34–2.20 wt%),  $TiO_2$  (<0.40 wt%), FeO (7.25–8.64 wt%), and  $Na_2O$  (0.05–0.22 wt%) contents, with higher Mg# (77 to 84). Actinolite also shows variable Zr/Hf (34.9 to 118.6), and Sr/Y ratios (7.8 to 83.5).

#### Cr-spinel

Cr-Spinel also forms inclusions in amphibole. The dominant spinel composition is high MgO (6.92–10.89 wt%), with variable Cr# (atomic  $Cr/[Cr + Al] \times 100$ ) of 53–58 and Mg# of 27–42.

**TABLE 1.** Bulk-rock major- and trace-element compositions of the Zhazhalong xenoliths and host granites

Sample:	HR2013-2	HR2013-3	HR2013-4	HR2013-5	HR2013-7	HR2013-8	HR2013-10	HR2013-11
Latitude, °N	30.0938	30.0938	30.0938	30.0938	30.0938	30.0938	30.0938	30.0938
Longitude, °E	88.8642	88.8642	88.8642	88.8642	88.8642	88.8642	88.8642	88.8642
Lithology	Granite	Granite	Granite	Granite	Xenolith	Xenolith	Xenolith	Xenolith
<b>Major oxides (wt%)</b>								
SiO <sub>2</sub>	70.12	74.15	70.96	72.14	45.95	42.41	44.96	45.93
TiO <sub>2</sub>	0.24	0.16	0.25	0.21	1.12	1.27	1.18	1.19
Al <sub>2</sub> O <sub>3</sub>	13.01	12.06	12.70	12.95	13.59	13.00	13.70	13.97
TFe <sub>2</sub> O <sub>3</sub>	2.17	1.46	2.30	1.37	9.77	10.46	9.40	9.58
MnO	0.21	0.32	0.24	0.16	0.48	0.42	0.41	0.49
MgO	1.01	1.00	1.07	0.93	10.97	11.37	9.58	10.28
CaO	1.76	1.21	1.65	1.47	7.52	11.90	10.40	7.86
Na <sub>2</sub> O	0.19	0.11	0.14	0.18	0.59	0.63	0.60	0.45
K <sub>2</sub> O	6.65	5.54	6.00	6.69	3.82	1.75	3.33	3.86
P <sub>2</sub> O <sub>5</sub>	0.08	0.05	0.08	0.07	0.49	0.59	0.45	0.52
LOI	4.54	3.83	4.58	3.73	5.15	5.62	5.44	5.36
Total	99.97	99.90	99.97	99.90	99.45	99.42	99.45	99.49
<b>Trace elements (ppm)</b>								
Rb	337	342	328	362	159	78	146	191
Sr	59.8	55.0	44.7	47.4	298	378	384	333
Co	2.51	2.18	2.14	1.48	45.3	50.9	44.4	50.0
Ni	1.34	2.04	1.87	1.69	189	213	168	194
Cu	4.28	12.10	2.60	2.14	12.5	12.2	13.7	64.8
Zn	20.4	14.2	28.9	15.6	123	120	108	144
Nb	13.7	9.78	13.6	12.1	16.4	14.4	16.2	17.2
Ba	414	205	229	323	3563	1726	2891	3693
Ta	2.30	1.73	1.87	1.81	1.50	0.94	1.03	1.16
Pb	56.6	62.4	54.9	56.0	34.9	13.9	28.7	46.5
Th	60.1	33.6	60.4	46.3	29.1	23.0	29.2	32.0
U	11.1	13.2	10.8	10.2	4.11	3.21	4.13	4.09
Zr	51.9	58.5	74.4	48.5	139	121	149	158
Hf	2.10	2.09	2.62	2.13	3.88	4.01	4.29	4.75
Y	21.3	12.7	21.4	16.1	22.6	24.7	24.1	25.6
Li	28.9	10.1	21.6	10.5	24.7	22.5	20.9	28.8
Be	3.00	2.06	2.50	3.36	1.37	1.16	1.46	2.92
Sc	5.16	3.86	5.10	4.17	26.0	31.8	26.9	29.8
V	14.4	9.57	14.9	13.8	219	262	226	245
Cr	4.76	3.19	4.97	4.49	506	585	489	563
Mo	1.02	1.75	0.96	0.54	0.13	0.20	0.14	0.13
Sb	0.64	1.43	0.62	0.76	0.36	0.58	0.43	0.53
Cs	8.67	15.70	7.35	8.11	36.5	23.7	29.6	24.2
W	3.41	1.09	3.44	2.41	1.39	2.47	2.23	3.30
Tl	2.97	2.64	3.41	3.14	2.82	1.32	2.45	3.14
La	68.5	30.6	69.5	42.5	88.8	82.2	91.4	99.4
Ce	128	56	131	79	138	133	142	154
Pr	14.2	6.34	14.6	8.94	13.9	14.2	14.4	15.6
Nd	50.2	23.0	51.3	32.0	48.2	50.8	49.1	53.1
Sm	8.82	4.12	8.92	5.83	7.13	7.80	7.31	7.80
Eu	0.72	0.50	0.61	0.54	1.59	1.89	1.70	1.82
Gd	6.76	3.16	6.70	4.43	6.16	6.78	6.64	6.81
Tb	1.05	0.55	1.16	0.71	0.95	1.13	1.05	0.96
Dy	4.64	2.45	4.68	3.16	4.37	5.26	4.50	4.84
Ho	0.70	0.45	0.76	0.53	0.81	0.86	0.85	0.83
Er	2.38	1.39	2.10	1.88	2.24	2.17	2.02	2.41
Tm	0.29	0.22	0.33	0.29	0.30	0.35	0.37	0.35
Yb	2.13	1.58	1.87	1.86	2.26	2.01	2.37	2.27
Lu	0.26	0.25	0.31	0.25	0.34	0.29	0.35	0.35

Note: LOI is loss on ignition.

## DISCUSSION

### A cumulate origin for the Zhazhalong xenoliths

The occurrence of amphibole-rich xenoliths in subduction-related igneous rocks is widely documented, and they are particularly common in island arcs (e.g., Arculus and Wills 1980; Davidson and Wilson 2011). Several possible explanations have been proposed for the origin of these xenoliths, including phenocryst clusters, entrained fragments of wall rocks or deep

► **FIGURE 3.** Chondrite-normalized (Sun and McDonough 1989) REE patterns for amphibole, whole-rock xenoliths, and liquids in equilibrium with amphibole, with the latter calculated using the Shimizu et al. (2017) partitioning model. (Color online.)

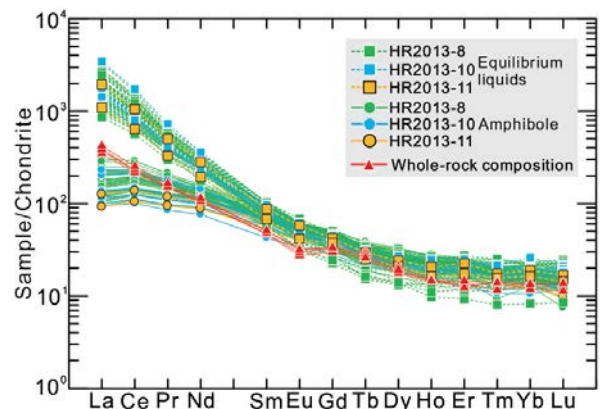


**TABLE 2.** Representative major- and trace-element compositions of amphibole

Sample	HR2013-8										HR2013-10					HR2013-11		
	s8	s23	s24	s26	s27	s35	s36	s42	s56	s59	s18	s19	s20	s21	s22	s23	s11	s17
Notes	mantle	core	rim	core	core	core	rim	core	core	rim	rim	core	core	core	core	core		
	<b>Oxide contents (wt%)</b>																	
SiO <sub>2</sub>	39.97	40.16	40.73	39.74	39.46	39.78	42.73	39.39	39.68	42.00	40.97	38.71	39.28	38.52	38.22	39.53	39.92	38.09
TiO <sub>2</sub>	1.87	1.43	1.40	2.69	2.81	1.68	0.57	3.06	2.53	1.47	0.88	2.69	2.59	2.50	2.61	2.51	1.92	3.14
Al <sub>2</sub> O <sub>3</sub>	13.53	13.33	13.72	13.47	13.73	13.65	11.86	13.75	13.48	11.78	13.16	13.94	13.90	14.21	13.85	13.73	13.66	13.52
FeO	11.63	11.91	11.83	10.89	10.44	11.23	10.99	9.89	10.51	11.08	11.35	11.35	11.23	11.15	11.11	10.95	11.25	10.80
MnO	0.18	0.23	0.24	0.16	0.13	0.16	0.23	0.09	0.15	0.18	0.18	0.11	0.11	0.12	0.13	0.12	0.14	0.11
MgO	14.59	15.04	15.35	15.54	15.01	15.10	16.76	15.63	15.31	15.88	15.60	14.63	14.53	14.71	14.12	15.13	15.16	14.34
CaO	12.07	11.78	11.93	11.67	11.82	11.99	11.47	12.27	12.11	12.15	11.69	12.00	12.10	12.12	12.18	12.09	12.16	12.13
Na <sub>2</sub> O	2.20	2.26	2.46	2.31	2.34	2.28	2.26	2.14	2.16	1.84	2.24	2.13	2.15	2.29	2.31	2.19	2.25	2.26
K <sub>2</sub> O	0.88	0.74	0.83	0.85	0.93	1.05	0.74	1.39	1.09	0.77	1.05	1.24	1.30	1.27	1.25	1.21	1.21	1.09
F	b.d.l.	0.13	0.25	0.21	0.22	b.d.l.	0.27	b.d.l.	0.22	b.d.l.	b.d.l.	0.10	b.d.l.	b.d.l.	b.d.l.	b.d.l.	b.d.l.	b.d.l.
Cl	0.07	0.08	0.12	0.05	0.06	0.05	0.07	0.03	0.05	0.06	0.05	0.04	0.04	0.03	0.04	0.03	0.03	0.04
Total	96.98	96.99	98.72	97.48	96.83	96.95	97.83	97.62	97.18	97.19	97.16	96.87	97.21	96.92	95.82	97.48	97.69	95.51
	<b>Trace element contents (ppm)</b>																	
P	367	146	222	208	292	204	230	131	193	178	168	207	202	150	147	178	180	158
V	414	320	308	432	457	332	206	477	407	328	280	424	435	464	437	455	395	416
Cr	9.74	91.5	148.5	5.03	10.5	15.9	180	171	14.8	34.4	90.7	41.3	23.0	18.0	12.3	13.5	178	198
Co	57.6	48.7	49.2	55.4	54.4	53.1	52.5	60.9	54.3	54.3	47.8	53.0	54.4	57.5	56.5	59.1	53.8	55.6
Ni	104	56.9	55.7	73.3	74.7	102	140	178	73.5	100	275	183	163	102	88.8	119	179	134
Cu	0.18	0.40	b.d.l.	0.25	0.25	0.07	0.17	0.26	0.41	0.29	0.20	0.32	0.27	0.25	0.57	0.03	0.37	0.30
Zn	88.3	85.5	83.7	54.1	51.8	65.8	87.0	41.8	56.5	78.6	84.2	56.2	55.3	54.7	52.0	49.9	52.8	40.5
Rb	7.90	4.63	3.60	4.72	5.98	6.73	4.73	8.54	8.74	5.29	7.65	7.53	8.80	14.29	13.00	10.09	9.45	6.09
Sr	633	485	537	585	645	455	398	599	519	481	491	497	508	519	493	523	459	513
Y	37.6	32.9	42.0	33.2	35.3	34.7	31.1	25.1	33.4	36.2	32.4	30.2	29.6	31.9	29.1	30.9	30.6	28.9
Zr	145	132	218	137	141	119	162	81	119	134	160	126	124	110	98	126	113	110
Nb	13.7	18.1	26.3	13.8	12.3	12.9	24.7	8.0	10.8	16.5	18.0	11.5	11.3	8.75	8.88	9.65	11.5	11.4
Mo	0.05	0.03	0.17	b.d.l.	b.d.l.	0.17	0.11	0.09	b.d.l.	0.13	0.28	0.05	0.08	0.03	0.11	b.d.l.	0.08	0.14
Cs	2.54	0.18	0.01	1.60	1.80	0.49	2.32	1.06	1.76	0.11	3.31	0.22	1.07	3.44	2.75	1.43	1.32	0.12
Ba	1068	750	782	927	1112	780	567	1679	1179	777	862	1433	1485	1521	1301	1407	1086	1151
La	42.8	47.2	41.7	25.3	37.7	34.2	40.6	23.7	29.3	38.2	54.6	32.9	31.8	27.2	23.4	27.1	29.7	21.9
Ce	116	132	122	76.8	104	103	116	69.4	87.8	110	143	90.6	89.5	77.2	67.5	76.1	83.7	64.1
Pr	15.2	16.6	16.1	10.5	13.9	13.3	14.3	9.16	11.6	14.8	16.9	11.9	11.6	10.5	9.31	10.4	11.2	8.95
Nd	65.5	64.8	66.9	48.2	59.1	58.1	56.6	41.9	52.9	61.4	66.6	53.1	50.8	47.0	42.0	45.8	50.4	41.0
Sm	12.6	10.9	11.6	10.1	12.9	11.4	8.8	8.2	10.8	11.5	9.9	10.4	10.0	9.7	8.8	9.8	9.5	8.3
Eu	3.49	3.18	3.33	2.85	3.15	2.75	2.67	2.37	2.74	3.14	2.75	2.48	2.83	2.74	2.29	2.44	2.82	2.24
Gd	10.7	8.41	10.4	9.18	10.6	8.60	6.58	7.67	9.00	8.95	7.64	7.82	8.47	7.88	7.48	8.28	8.15	7.90
Tb	1.39	1.00	1.30	1.25	1.29	1.05	0.95	0.93	1.11	1.21	0.97	1.11	1.07	1.05	1.05	1.11	1.10	1.01
Dy	7.56	6.09	7.81	6.41	7.89	7.09	5.38	6.04	6.64	6.97	5.08	5.96	6.11	6.23	5.77	5.92	6.17	5.72
Ho	1.27	1.20	1.59	1.08	1.43	1.30	1.06	0.88	1.23	1.32	1.09	1.13	1.09	1.22	1.02	1.14	1.14	0.95
Er	3.59	3.62	4.34	3.62	3.38	3.40	2.99	2.38	3.27	3.80	3.46	2.98	3.05	3.37	2.89	3.04	3.37	2.73
Tm	0.43	0.44	0.46	0.42	0.45	0.43	0.42	0.24	0.41	0.51	0.48	0.38	0.36	0.41	0.29	0.37	0.36	0.34
Yb	2.77	2.64	3.40	2.46	2.89	2.92	2.79	2.17	2.74	2.96	2.85	2.23	2.25	2.11	2.10	2.50	2.36	2.12
Lu	0.38	0.38	0.46	0.31	0.33	0.40	0.44	0.19	0.34	0.39	0.36	0.29	0.33	0.32	0.30	0.32	0.28	0.25
Hf	5.08	3.35	3.70	4.40	5.19	3.40	4.20	3.43	3.77	3.73	4.16	4.17	4.54	3.70	3.38	4.39	3.58	4.98
Ta	0.80	0.82	1.03	0.69	0.76	0.67	0.88	0.39	0.57	0.66	0.96	0.62	0.66	0.54	0.49	0.55	0.61	0.54
W	0.04	0.01	0.01	0.05	0.01	0.01	b.d.l.	b.d.l.	0.01	0.01	0.18	b.d.l.	0.03	0.46	b.d.l.	b.d.l.	0.01	0.05
Pb	4.81	5.32	5.78	4.13	5.12	4.36	4.40	3.63	4.22	5.18	4.24	3.98	4.12	4.70	4.38	3.66	4.56	3.50
Th	3.52	1.94	1.44	0.99	2.89	1.37	2.41	1.04	1.22	1.51	2.84	1.29	1.45	5.47	3.84	1.49	4.19	0.65
U	0.13	0.16	0.13	0.10	0.12	0.13	0.14	0.08	0.10	0.16	0.60	0.11	0.10	0.13	0.23	0.09	0.10	0.06

Note: b.d.l. = below detection limit.

basement, and xenoliths of cumulate material (e.g., Tollan et al. 2012). The framework of euhedral amphibole grains in the xenoliths studied here is consistent with an igneous origin. Formation of amphibole-rich lithologies can be attributed to two mechanisms. One possibility is that they formed by nucleation, growth, and settling of amphibole crystals from parental liquids (e.g., Davidson et al. 2007). An alternative is that they developed through a peritectic reaction whereby early crystallized clinopyroxene or olivine reacted with residual or injected melts (e.g., Smith 2014; Humphreys et al. 2019a). Many studies have presented petrographic evidence supporting the formation of amphibole by reaction between melt and clinopyroxene (e.g., Smith 2014; Cooper et al. 2016; Klaver et al. 2017; Melekhova et al. 2017; Stamper et al. 2014). However, the following lines of evidence suggest that the Zhazhalong amphibole-dominated xenoliths formed by direct crystal accumulation: (1) the xenoliths are characterized by a framework of idiomorphic amphibole

grains (Figs. 2a and 2b); (2) the mineral-whole-rock Fe–Mg exchange coefficient (Fig. 5a), which is an effective signature of crystal accumulation (Putirka 2016; Barnes et al. 2016), indicates a cumulate origin for the xenoliths; (3) the REE compositions of the xenoliths, which are enriched in LREEs relative to HREEs, are similar to those of the amphibole itself (Fig. 3); (4) the melts that are inferred to have been in equilibrium with amphibole have similar compatible trace-element contents, but significantly higher incompatible trace-element contents, compared with the xenoliths (as discussed in the next section); and (5) the SiO<sub>2</sub> content of the melt in equilibrium with amphibole can be estimated using the amphibole composition alone (Ridolfi et al. 2010; Erdmann et al. 2014; Putirka 2016), with calculations showing that the Zhazhalong amphibole crystallized from basaltic to andesitic magmas (46.4–66.4 wt% SiO<sub>2</sub>; Fig. 5b), which contrasts with the whole-rock compositions of the xenoliths (42.41–45.95 wt% SiO<sub>2</sub>).

**TABLE 3.** Major -and trace-element compositions of actinolite

Sample	HR2013-8							
Spot	s10	s40	s41	s45	s48	s63	s64	s72
<b>Oxide contents (wt%)</b>								
SiO <sub>2</sub>	54.22	55.96	56.01	54.73	55.14	55.80	55.41	55.49
TiO <sub>2</sub>	b.d.l.	0.04	0.03	b.d.l.	0.04	b.d.l.	b.d.l.	b.d.l.
Al <sub>2</sub> O <sub>3</sub>	2.20	0.48	0.34	0.36	0.46	0.60	0.73	0.39
FeO	8.38	7.89	7.98	7.90	8.46	8.64	7.25	8.27
MnO	0.36	0.23	0.21	0.18	0.22	0.18	0.17	0.25
MgO	19.55	20.28	20.74	19.77	19.56	19.78	20.76	19.94
CaO	13.01	13.25	13.25	13.18	13.05	12.94	13.27	13.05
Na <sub>2</sub> O	0.14	0.16	0.11	0.05	0.12	0.22	0.12	0.15
K <sub>2</sub> O	0.06	0.02	0.02	0.01	0.03	0.04	b.d.l.	0.03
F	b.d.l.	b.d.l.	b.d.l.	b.d.l.	b.d.l.	b.d.l.	b.d.l.	b.d.l.
Cl	b.d.l.	0.01	b.d.l.	b.d.l.	b.d.l.	b.d.l.	b.d.l.	0.01
Total	97.91	98.31	98.69	96.19	97.07	98.19	97.70	97.55
<b>Trace element contents (ppm)</b>								
P	35.7	57.9	4.42	96.3	30.6	37.2	17.4	28.6
V	98.8	111	132	125	138	101	106	109
Cr	660	745	318	503	1060	352	586	263
Co	78.5	54.9	53.7	53.6	55.4	56.8	57.4	53.6
Ni	1034	883	845	880	524	691	711	872
Cu	0.10	0.43	0.05	0.11	0.08	0.05	0.21	b.d.l.
Zn	165	76.9	91.1	68.7	85.6	90.0	92.0	74.2
Rb	2.32	0.28	0.33	0.06	0.67	0.46	0.24	0.13
Sr	4.84	17.6	12.4	9.10	8.20	5.48	6.85	9.81
Y	0.25	0.73	0.15	0.48	0.48	0.71	0.53	0.19
Zr	1.51	4.65	7.43	0.52	4.74	7.23	3.81	0.68
Nb	0.04	0.03	b.d.l.	0.04	0.02	0.03	0.01	0.04
Mo	0.09	b.d.l.	b.d.l.	0.01	0.05	0.12	0.10	0.00
Cs	6.41	0.44	0.32	0.10	2.12	1.68	0.42	0.19
Ba	2.10	4.56	0.38	0.79	1.19	0.38	0.58	0.24
La	0.05	0.17	0.06	0.06	0.06	0.03	0.03	0.07
Ce	0.12	0.22	0.16	0.14	0.12	0.14	0.09	0.15
Pr	0.02	0.06	0.02	0.01	0.02	0.02	0.02	0.02
Nd	0.07	0.08	0.22	0.05	b.d.l.	0.09	0.10	0.03
Sm	b.d.l.	0.02	0.07	0.02	b.d.l.	0.04	0.02	b.d.l.
Eu	0.01	0.03	0.02	b.d.l.	0.01	0.01	0.01	b.d.l.
Gd	b.d.l.	0.09	0.02	b.d.l.	0.03	0.12	0.10	0.05
Tb	b.d.l.	0.03	b.d.l.	0.01	b.d.l.	0.01	0.01	b.d.l.
Dy	b.d.l.	0.14	0.04	0.03	0.05	0.07	0.07	0.01
Ho	0.01	0.02	0.01	0.01	0.02	0.02	0.01	0.01
Er	0.01	0.06	0.02	0.07	0.08	0.11	0.12	0.03
Tm	0.01	0.05	0.01	0.02	0.01	0.01	0.02	0.01
Yb	0.09	0.25	0.28	0.14	0.16	0.27	0.18	0.09
Lu	0.01	0.05	0.09	0.02	0.05	0.12	0.07	0.04
Hf	0.04	0.04	0.21	0.01	0.09	0.10	0.05	0.01
Ta	0.01	0.01	b.d.l.	0.01	0.01	b.d.l.	b.d.l.	0.01
W	0.07	b.d.l.	b.d.l.	b.d.l.	0.02	0.06	b.d.l.	0.01
Pb	0.81	0.67	0.27	1.64	3.99	0.41	0.41	0.18
Th	1.17	0.83	0.51	0.40	0.31	0.32	0.18	0.12
U	0.03	0.05	0.00	0.04	0.04	0.01	0.03	0.01

Note: b.d.l. = below detection limit.

Although the Zhazhalong xenoliths are likely to be of cumulate origin, potential reaction-replacement processes prior to amphibole accumulation can also be recognized. Some amphibole grains have a core of actinolite that is surrounded by lower-silica, more aluminous calcic amphibole similar in composition to

**TABLE 4.** Major-element compositions of Cr-spinel

Sample	HR2013-8				
Spot	s77	s78	s79	s81	s82
<b>Oxide contents (wt%)</b>					
SiO <sub>2</sub>	0.07	0.07	0.06	0.08	0.07
TiO <sub>2</sub>	0.76	0.89	0.78	0.84	0.80
Al <sub>2</sub> O <sub>3</sub>	19.36	22.02	18.78	19.78	19.42
FeO	26.33	29.03	32.79	28.23	28.73
MnO	0.40	0.47	0.97	0.45	0.49
MgO	10.89	9.83	6.92	9.73	9.42
CaO	0.05	b.d.l.	0.02	0.07	0.04
Cr <sub>2</sub> O <sub>3</sub>	40.54	36.89	39.46	39.38	40.19
Total	98.39	99.20	99.78	98.56	99.15

Note: b.d.l. = below detection limit.

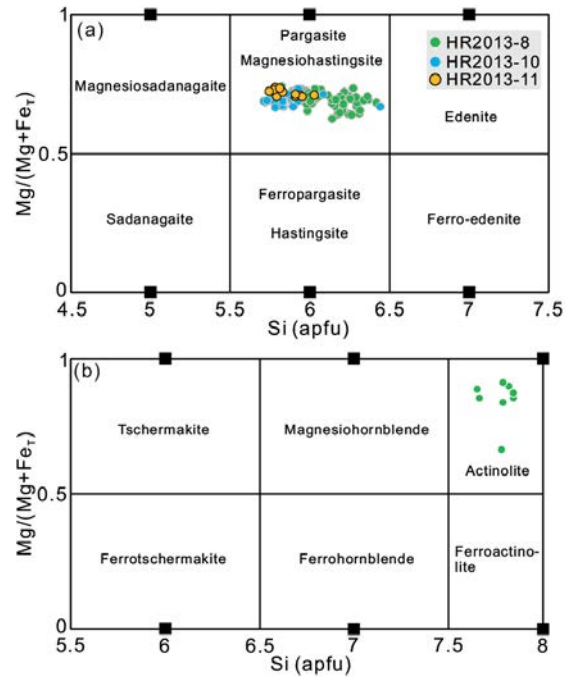


**FIGURE 4.** (a) Amphibole compositions. (b) Actinolite compositions. Amphibole cation site occupancies were estimated using the method of Putirka (2016). Classification and nomenclature follow Leake et al. (1997). (Color online.)

that of other idiomorphic amphiboles in the xenoliths (Fig. 2d). Actinolite is generally expected to be a product of subsolidus reaction, and overprints earlier amphibole along grain boundaries, cracks, and cleavage planes (Martin 2007). Actinolitic cores surrounded by aluminous, calcic amphibole is the reverse of that expected due to magma crystallization (Martin 2007). A probable explanation is that the core is a pseudomorph after primary pyroxene or olivine (e.g., Compton 1958; Zhang et al. 2015; Humphreys et al. 2019a). Thus, the actinolite crystals within the interior of some amphibole grains may represent the replacement of olivine due to reaction with hydrous melts, as evidenced by the significantly high contents of Cr and Ni in the cores (Table 3). This interpretation is also consistent with the high Cr and Ni whole-rock contents of the Zhazhalong xenoliths (Table 1).

#### Physical conditions for amphibole accumulation

Studies of plutonic xenoliths have provided important insights into deep-crustal processes, not only in arc magmatic systems (e.g., Arculus and Wills 1980; Tollan et al. 2012; Cooper et al. 2016; Melekhova et al. 2017; Stamper et al. 2014; Chin et al. 2018) but also in continental rift settings (e.g., Chin 2018). Here, we use multiple thermodynamic calibrations to place constraints on the formation of the Zhazhalong cumulate lithologies. Calibrations based on a specific mineral assemblage or amphibole-liquid exchange equilibria are not applicable to cumulate rocks because of the lack of appropriate mineral assemblages and knowledge of the composition of parental melts. Amphibole is abundant in the Zhazhalong xenoliths; thus empirical thermobarometric formulas depending on the compositions of individual am-

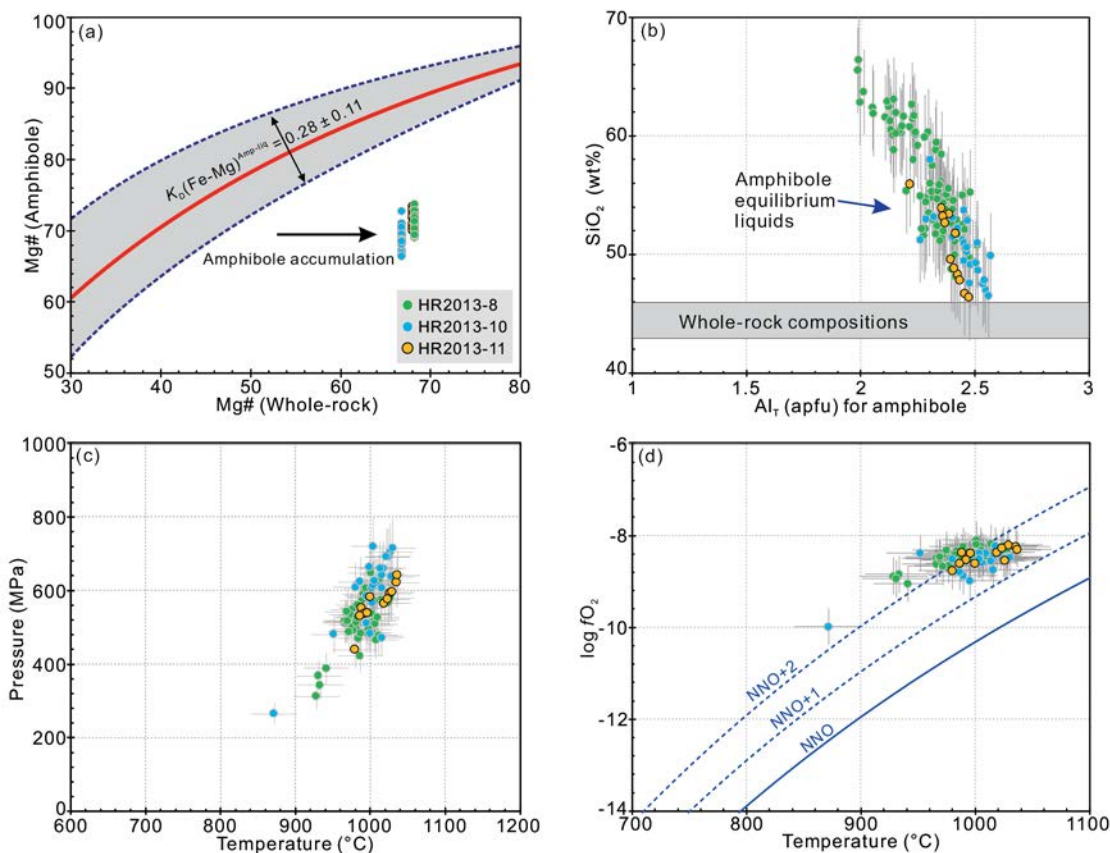


**FIGURE 5.** (a) Tests of amphibole–liquid Fe–Mg exchange equilibrium.  $K_D$  values in the range  $0.28 \pm 0.11$  (Putirka 2016) are regarded to be in chemical equilibrium. (b) Relationship between  $Al_{total}$  in amphibole and the predicted  $SiO_2$  content of coexisting liquid. The range of compositions of the xenoliths is shown by the horizontal gray bar. (c and d) Calculated temperature, pressure, and oxygen fugacity based on amphibole compositions. Oxygen fugacity and pressure were calculated using the method of Ridolfi et al. (2010). The pressure estimates should be treated with caution. Temperatures and the  $SiO_2$  contents of coexisting liquids were calculated using Equations 5 and 10 of Putirka (2016), respectively. The calibration of the nickel–nickel oxide (NNO) buffer is taken from O'Neill and Pownceby (1993). (Color online.)

phiboles were employed to estimate the conditions of crystal accumulation (Ridolfi et al. 2010; Putirka 2016). Given the test of Erdmann et al. (2014), oxygen fugacity was estimated using the method of Ridolfi et al. (2010); temperatures, and the  $SiO_2$  contents of coexisting liquids were calculated using the equations of Putirka (2016). Figures 5b–5d shows the full range of equilibrium liquid  $SiO_2$  contents, temperatures, pressures, and oxygen fugacities for the Zhazhalong cumulate xenoliths. The modeled temperatures are in the range 857–1034 °C (Fig. 5c), and oxygen fugacity is 0.4 to 1.9 log units above the nickel–nickel oxide buffer ( $\Delta NNO = 0.4$ –1.9; Fig. 5d). As mentioned above, the calculated equilibrium liquids have  $SiO_2$  contents of 46.4–66.4 wt% (Fig. 5b). Application of the Ridolfi et al. (2010) model gives pressures from 312 to 692 MPa (Fig. 5c). However, for low-Si amphibole that crystallizes from mafic to intermediate magmas, the Ridolfi et al. (2010) model overestimates pressure (Erdmann et al. 2014). Thus, the Zhazhalong xenoliths likely formed at mid-crustal depths.

### Compositions of the equilibrium liquids

Understanding of the compositional relationship between cumulates and their coexisting liquids is derived mainly from ex-

perimental studies (e.g., Müntener and Ulmer 2018). Approaches based on natural examples are rare because of the difficulty of predicting liquid compositions based on that of the cumulate. In addition, although the thermodynamic modeling software MELTS has been widely used to track the evolution of mafic–intermediate magmas (Ghiorso and Sack 1995), the algorithms in MELTS cannot easily deal with amphibole fractionation (Ghiorso 1997). Here, we attempt to provide a quantitative assessment of the chemical compositions of the liquids that coexisted with the Zhazhalong cumulates.

A series of empirical chemometric equations for calculating the major-element compositions of liquids in equilibrium with amphibole based on an expanded data set of experimental results were proposed by Zhang et al. (2017) and updated by Humphreys et al. (2019b). Using these equations, the melt major-element compositions (i.e.,  $SiO_2$ ,  $TiO_2$ ,  $Al_2O_3$ ,  $FeO_{total}$ ,  $MgO$ ,  $CaO$ , and  $K_2O$  as wt%) were obtained (Supplemental<sup>1</sup> Table S1). Based on amphiboles from the Zhazhalong cumulate xenoliths, the calculated melts have 48.6–65.7 wt%  $SiO_2$ , 0.2–1.5 wt%  $TiO_2$ , 15.2–19.1 wt%  $Al_2O_3$ , 3.4–11.8 wt%  $FeO_{total}$ , 1.2–7.7 wt%  $MgO$ , 3.5–9.6 wt%  $CaO$ , 0.9–3.3 wt%  $K_2O$ , and  $Mg\#$  of 32–58 (Supplemental<sup>1</sup> Table S1). A comparison of the  $SiO_2$  contents

of the melts using the formulation of Putirka (2016) with those using the method of Zhang et al. (2017) shows excellent agreement (Fig. 6a). To assess the reliability of the calculated melt compositions, we performed a test for amphibole–liquid Fe–Mg exchange equilibrium, following the approach of Putirka (2016). The Fe–Mg exchange coefficient  $K_D(\text{Fe–Mg})^{\text{amphibole–liquid}}$  (hereafter  $K_D$ ) is defined as:

$$K_D = \frac{X_{\text{FeOt}}^{\text{Amp}} / X_{\text{MgO}}^{\text{Amp}}}{X_{\text{FeOt}}^{\text{Liquid}} / X_{\text{MgO}}^{\text{Liquid}}} \quad (1)$$

where FeOt represents total Fe as FeO. Amphibole–liquid pairs with  $K_D$  of  $0.28 \pm 0.11$  (Putirka 2016) were regarded to be in chemical equilibrium. As shown in Figure 6b, most amphibole–liquid pairs were in or near Fe–Mg exchange equilibrium. Thus, the Zhazhalong amphibole-rich cumulates likely crystallized from basaltic to andesitic magmas.

The most challenging issue in the calculation of trace-element compositions of liquids based on amphibole chemistry is that amphibole/melt partition coefficients can vary significantly under different conditions (Tiepolo et al. 2007), with the application of different partition coefficients producing diverse results (e.g., Barnes et al. 2017). Trace-element partitioning between amphibole and liquid is sensitive to temperature, pressure, crystal chemistry, and melt composition (Tiepolo et al. 2007), so application of a single set of experimentally determined partition coefficients to natural samples is associated with large uncertainties. Parameterized trace-element-partitioning models may solve this difficulty (Brice 1975; Blundy and Wood 1994; Wood and Blundy 1997; Shimizu et al. 2017; Humphreys et al. 2019b). The partitioning behavior of REEs is well understood and can be easily fitted by a lattice strain model (Blundy and Wood 1994; Shimizu et al. 2017). According to the model, the partition coefficients of trace elements between amphibole and liquid can be expressed as:

$$D_i^{\text{Amp–liquid}} = D_0 \exp \left[ - \frac{4EN_A}{RT} \left( \frac{r_0}{2} (r_0 - r_i)^2 - \frac{1}{3} (r_0 - r_i)^3 \right) \right] \quad (2)$$

where  $D_i$  and  $D_0$  are the theoretical and strain-free amphibole–liquid partition coefficients, respectively;  $r_0$  is the optimum radius of

the lattice site;  $r_i$  is the ionic radius of element;  $E$  is the effective Young's modulus;  $R$  is the gas constant (8.3145 J/mol·K);  $N_A$  is Avogadro's number; and  $T$  is the temperature in Kelvin. The parameters ( $D_0$ ,  $r_0$ , and  $E$ ) are a function of pressure, temperature, and composition, which Shimizu et al. (2017) quantified through a parameterized model based on amphibole compositions:

$$\ln D_0 = -4.21 + \frac{7.27 \times 10^4}{RT} + 1.52 X_{\text{Ti}}^{\text{Amp}} - 0.35 X_{\text{Mg}}^{\text{Amp}} - 1.83 X_{\text{Na}}^{\text{Amp}} - 2.95 X_{\text{K}}^{\text{Amp}} \quad (3)$$

$$r_0 = 1.043 - 0.039 X_{\text{Fm}}^{\text{Amp–M4}} \quad (4)$$

$$E = 337 \quad (5)$$

$$X_{\text{Fm}}^{\text{Amp–M4}} = X_{\text{Fe}^{2+}}^{\text{Amp–M4}} + X_{\text{Mn}^{2+}}^{\text{Amp–M4}} + X_{\text{Mg}}^{\text{Amp–M4}} \quad (6)$$

where  $X_{\text{Ti}}^{\text{Amp}}$ ,  $X_{\text{Mg}}^{\text{Amp}}$ ,  $X_{\text{Na}}^{\text{Amp}}$ , and  $X_{\text{K}}^{\text{Amp}}$  are the number of cations (per 23 O atoms), and  $X_{\text{Fe}^{2+}}^{\text{Amp–M4}}$ ,  $X_{\text{Mn}^{2+}}^{\text{Amp–M4}}$ , and  $X_{\text{Mg}}^{\text{Amp–M4}}$  are the number of cations on the M4 site. Amphibole cation site occupancies and  $\text{Fe}^{2+}$  cation numbers were estimated using the method of Putirka (2016).

The calculated partition coefficients of REEs and Y for the Zhazhalong amphiboles are given in Supplemental Table S1 and shown in an Onuma diagram (Fig. 7a). Partition coefficients for other trace elements were predicted using the empirical scheme of Humphreys et al. (2019b), and only elements with good linear fits (adjusted  $R^2 > 0.6$ ) were utilized. Partition coefficients for La and Dy that were calculated using two independent methods are shown for comparison in Figures 7b and 7c, respectively. Overall, the partition coefficients that were calculated using the Humphreys et al. (2019b) model have values that are slightly higher than those calculated using the Shimizu et al. (2017) model. The partition coefficients for REEs and Y using the Shimizu et al. (2017) model and for Rb and Sr based on the Humphreys et al. (2019b) scheme were then employed to calculate the trace-element compositions of the liquids from which the Zhazhalong amphiboles crystallized. The compositions of the equilibrium liquids are characterized by enrichment of LREEs over HREEs and an absence of a negative Eu anomaly, comparable with the

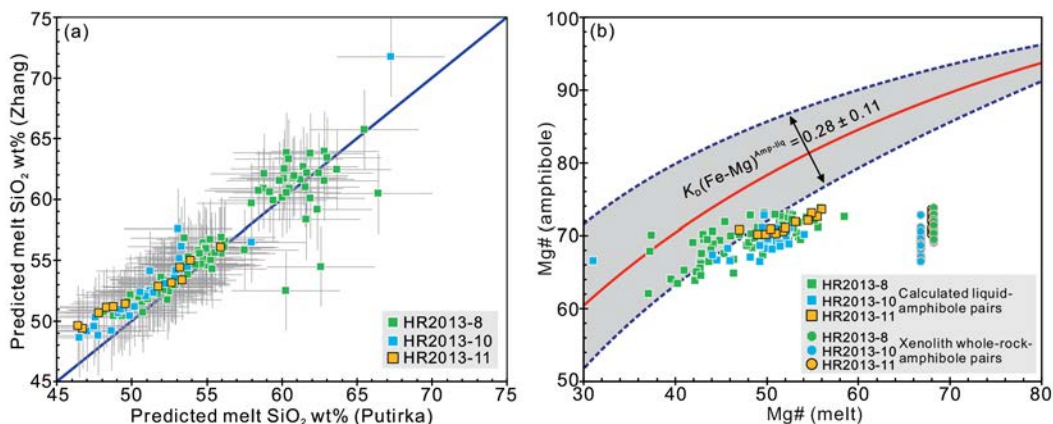


**FIGURE 6.** (a) Comparison of predicted liquid  $\text{SiO}_2$  contents using the equations of Putirka (2016) and Zhang et al. (2017). (b) Tests of amphibole–liquid Fe–Mg exchange equilibrium. Xenolith–amphibole pairs are also shown. (Color online.)

features observed in the amphiboles, albeit with higher LREE (Fig. 3) and Sr contents (Supplemental Table S1).

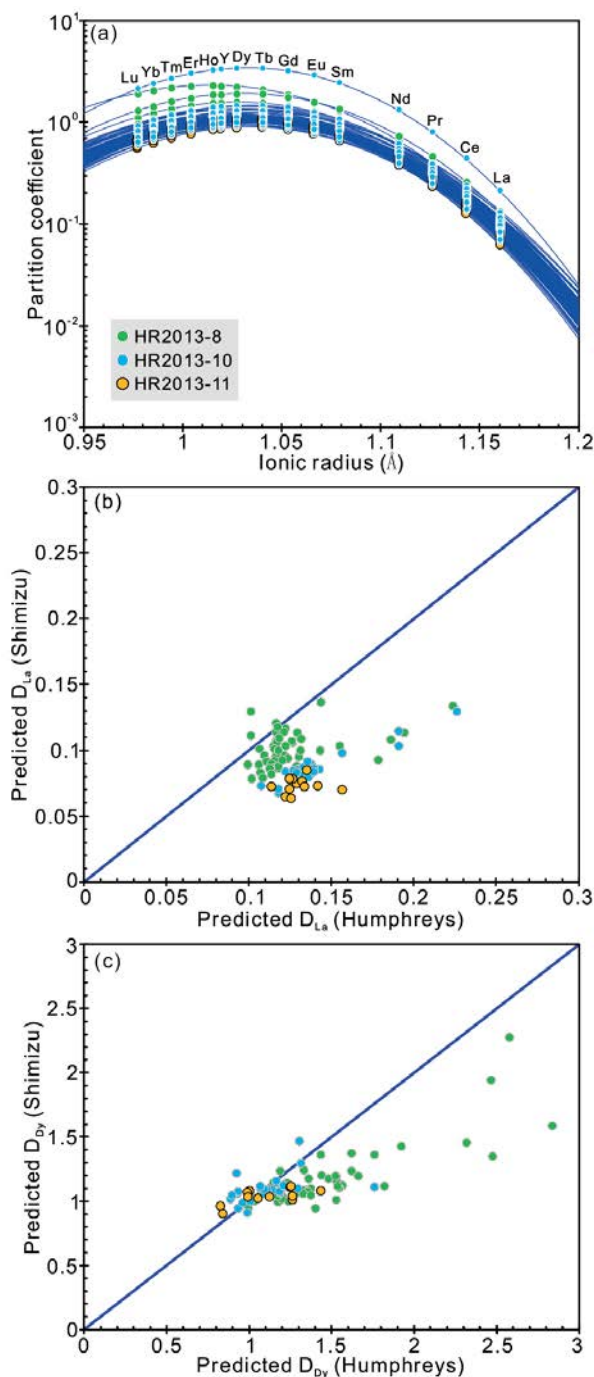
### The role of amphibole fractionation during magma evolution

Our study demonstrates that the role of amphibole-controlled fractionation on the evolving chemical of magmas can be assessed on the basis of an investigation of cumulates. Amphibole in the Zhazhalong cumulate xenoliths is characterized by low SiO<sub>2</sub> and high TiO<sub>2</sub> contents. Thus, precipitation of amphibole can drive derivative melts toward higher SiO<sub>2</sub> and lower TiO<sub>2</sub> contents. The wide range of calculated temperatures (857 to 1037 °C; Fig. 5c) can be attributed to multiple factors, such as analytical errors, inherent uncertainties in the thermometric calculations, and crystallization temperatures. However, liquids in equilibrium with amphibole become successively enriched in incompatible elements (e.g., La; Fig. 8a) and depleted in compatible elements (e.g., Dy; Fig. 8b) with decreasing temperature. Thus, the variability in temperatures reflects mainly crystallization and/or post-cumulus overgrowths. Similar differentiation trends are not obvious in plots vs. amphibole Mg# (Figs. 8d and 8e). Amphibole Mg# is correlated positively not only with parental melt composition but also with H<sub>2</sub>O content and oxygen fugacity (Fig. 9a; Grove et al. 2003; Krawczynski et al. 2012). In the present study, decoupling between the Mg# of amphibole and temperature probably reflects an increase in oxygen fugacity with cooling (Fig. 9b).

The concentrations of compatible trace elements in the equilibrium liquids almost overlap with the whole-rock compositions of the xenoliths (such as Dy; Figs. 8b and 8e). In contrast, the concentrations of incompatible trace elements in the equilibrium liquids are significantly higher than in the xenoliths (such as La; Figs. 8a and 8d). This discrepancy may result from post-cumulus compaction and upward expulsion of evolved interstitial liquid that was enriched in incompatible trace elements. This process (i.e., solidification accompanied by compaction) has been recognized in many igneous cumulates (e.g., Meurer and Boudreau 1998). Following the approach of Meurer and Boudreau (1998), we estimated the trapped liquid fraction using trace elements (La, Ce, and Dy) whose partitioning behavior is well understood in this study. The results indicate that the weight proportion of trapped liquid varies from 12 to 20%. Although the Zhazhalong amphiboles are characterized by very high contents of some elements, such as Sr, there is no appreciable decrease in the Sr content of equilibrium liquid with decreasing temperature (Fig. 8c). Consequently, precipitation of amphibole had a negligible effect on the Sr composition of the residual liquid.

Trends of decreasing Dy/Yb and Dy/Dy\* ratios with increasing

SiO<sub>2</sub> are regarded as key evidence for amphibole fractionation during magma evolution (Davidson et al. 2007, 2013). To further test this hypothesis, we investigated Dy/Yb and Dy/Dy\* variations using the compositions of the cumulates studied here (Fig. 10). The modeled changes in the Dy/Yb and Dy/Dy\* ratios of derivative liquids and cumulates with increasing degrees of differentiation, assuming that amphibole was a major fractionating phase, are shown in Figure 10b. The results show apparently decreasing Dy/Yb and Dy/Dy\* ratios in the liquids with progressive removal of amphibole. Therefore, our results confirm that Dy/Yb and



► **FIGURE 7.** (a) Onuma diagram for REE and Y partition coefficients as a function of cation radius. Data marked by circles were calculated using the model of Shimizu et al. (2017). The blue lines are the best-fit parabola to the trivalent REEs and Y using the equation of the lattice strain model (Brice 1975; Blundy and Wood 1994; Wood and Blundy 1997). The lattice strain parameters  $D_0$ ,  $r_0$ , and  $E$  were obtained using the mineral composition model of Shimizu et al. (2017). Ionic radii are from Shannon (1976). (b) Comparison of predicted  $D_{La}$  using the models of Humphreys et al. (2019b) and Shimizu et al. (2017). (c) Comparison of predicted  $D_{Dy}$  using the models of Humphreys et al. (2019b) and Shimizu et al. (2017). (Color online.)

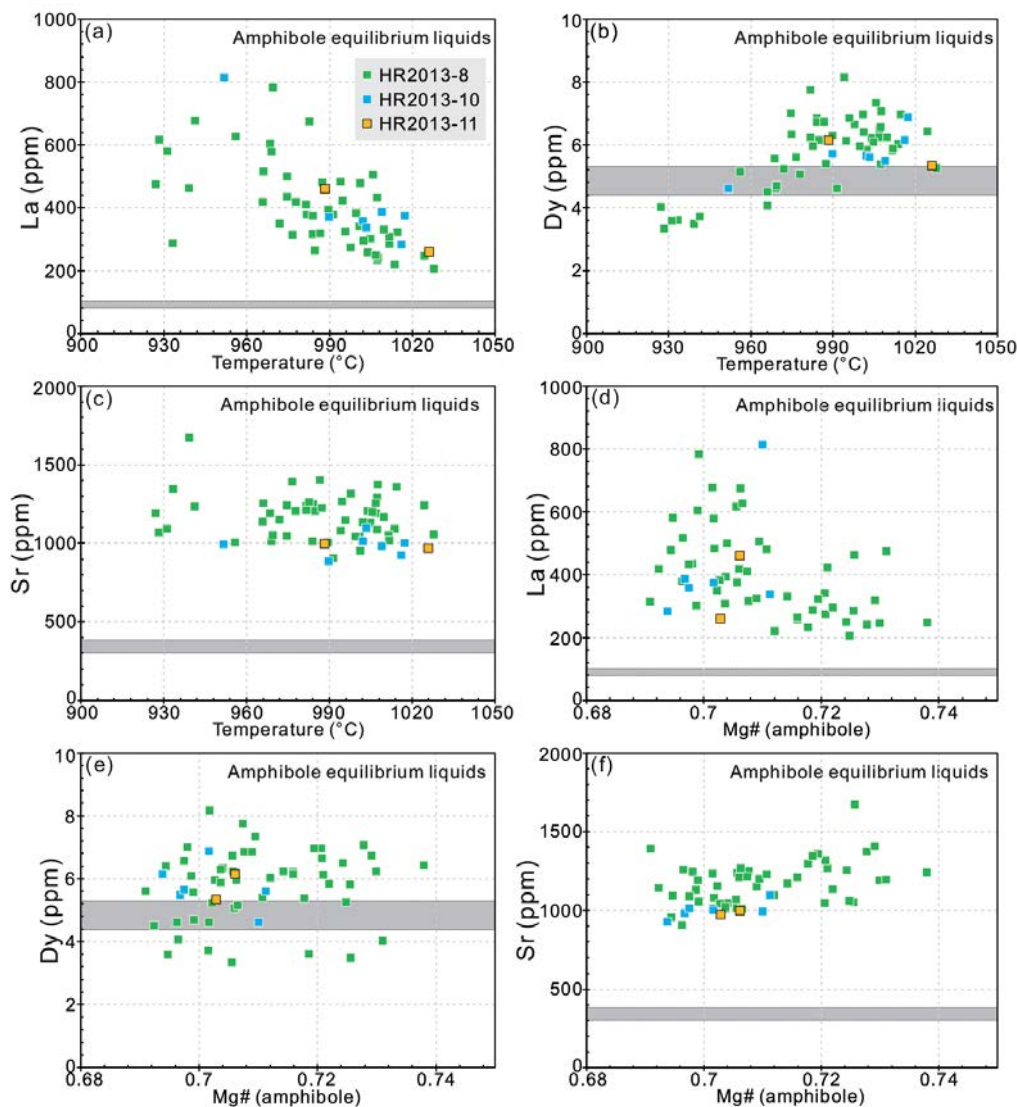


**FIGURE 8.** (a–c) Calculated La, Dy, and Sr concentrations of the equilibrium liquid as a function of temperature. (d–f) Calculated La, Dy, and Sr concentrations of the equilibrium liquid as a function of the Mg# of amphibole. (Color online.)

Dy/Dy\* ratios are robust geochemical fingerprints of amphibole crystallization during magma evolution.

It is also noteworthy that the amphiboles in this study have unusually high Sr ( $511 \pm 65$  ppm), Ba ( $944 \pm 261$  ppm), and LREE contents. The Sr contents of the equilibrium liquids range from 885 to 1402 ppm, based on the partitioning scheme of Humphreys et al. (2019b). Thus the parental melts of the Zhazhalong amphiboles were enriched in Sr, Ba, and LREEs (Supplemental<sup>1</sup> Table S1). These geochemical features have been observed in some island arc magmatic rocks (e.g., Sadofsky et al. 2008), which has generally been interpreted to reflect the incorporation of marine sediments into the magma sources (e.g., Othman et al. 1989; Plank and Langmuir 1993). The high contents of large-ion lithophile elements and LREEs, together with plenty of interstitial K-feldspars in the matrix of the xenoliths, suggest that the parent liquids were shoshonitic, which is a compositional series within

island arc magma systems (e.g., Stern et al. 1988; Bloomer et al. 1989) or post-collision magmatic settings (e.g., Turner et al. 1996). Only a small amount of the equilibrium melts is inferred to have been shoshonitic, with most belonging to the high K calc-alkaline series (Supplemental<sup>1</sup> Fig. S3), although the reason for this is unclear. In addition, the Zhazhalong amphibole-rich xenoliths have petrological similarities to appinite, which shows genetic relationships with some particular rock suites, such as high Ba–Sr granites and sanukitoids (e.g., Murphy 2013; Tiepolo and Tribuzio 2008). Our detailed study suggests that, at least in some cases, appinite suites could represent amphibole-rich cumulates derived from water-rich magmas.

## IMPLICATIONS

The Zhazhalong xenoliths provide a rare example of fragments of arc cumulates in which the crystal framework consists

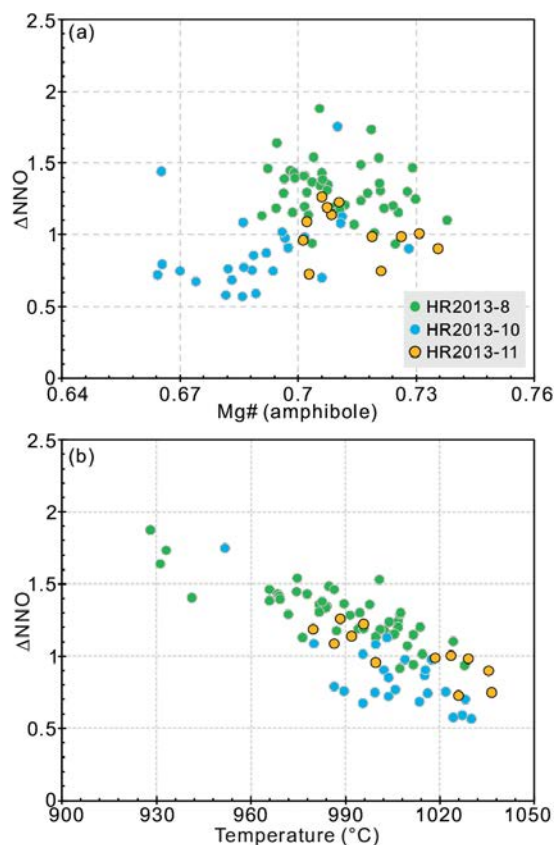


**FIGURE 9.** (a) Mg# of amphibole as a function of oxygen fugacity. Oxygen fugacity was constrained using the method of Ridolfi et al. (2010). (b) Temperature vs. oxygen fugacity. Temperatures were calculated by using Equation 5 of Putirka (2016). (Color online.)

mostly of amphibole. Several independent lines of evidence, including textural characteristics, Fe–Mg exchange coefficients, trace-element signatures, and equilibrium liquid compositions, indicate that the Zhazhalong xenoliths represent fragments of amphibole-rich cumulates formed by crystal accumulation in which trapped liquid fractions were ~12–20%. Actinolitic cores within amphibole grains represent reaction products of primary olivine with hydrous melt. Thermometry and oxybarometry based on amphibole compositions indicate that the temperatures of crystal accumulation ranged from 857 to 1014 °C, pressures from 312 to 692 MPa, and oxygen fugacities from 0.4 to 1.9  $\Delta$ NNO. The xenoliths likely formed at mid-crustal depths. The major- and trace-element compositions of the parent melts were also quantified. The results show that the Zhazhalong amphiboles crystallized from basaltic to andesitic (probably shoshonitic) magmas with SiO<sub>2</sub> contents of 46.4–66.4 wt%. The equilibrium liquids were also enriched in LREEs and Sr. The previous proposal that decreasing Dy/Yb and Dy/Dy\* ratios with increasing differentiation can be used as a signature of amphibole fractionation (Davidson et al. 2007, 2013) is supported by the investigation of cumulate xenoliths in the present study.

Our work permits a better understanding of the role of amphibole fractionation during magma evolution. Although the

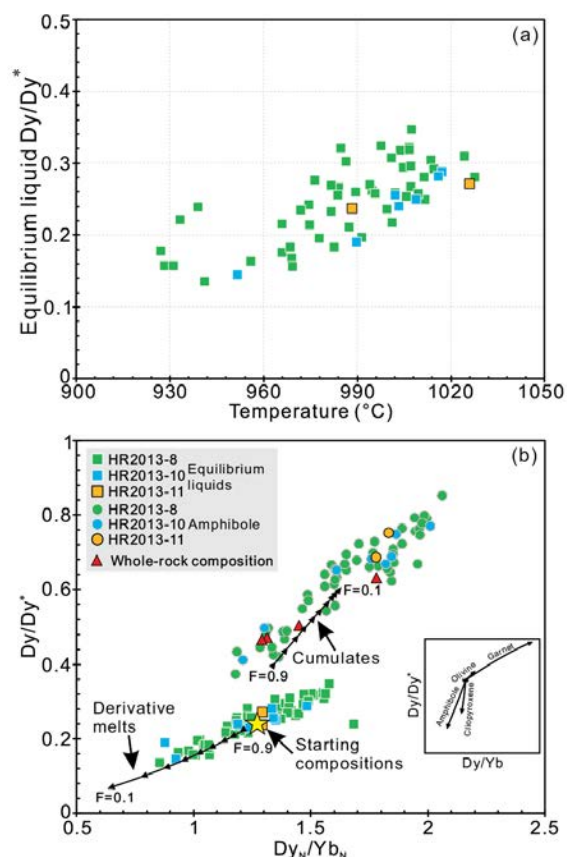


**FIGURE 10.** (a) Variation in Dy/Dy\* of the equilibrium liquid as a function of temperature. (b) Quantitative assessment of Dy/Yb and Dy/Dy\* with amphibole fractionation, using Rayleigh fractionation and our calculated partition coefficients. The calculations assume the average composition of liquids in equilibrium with amphiboles that have temperatures of >1000 °C as an initial composition, where Dy<sub>N</sub>/Yb<sub>N</sub> = 1.25 and Dy/Dy\* = 0.24. The average partition coefficients were  $D_{La} = 0.1$ ,  $D_{Dy} = 1.2$ , and  $D_{Yb} = 0.91$ .  $F$  represents melt fraction. (Color online.)

importance of amphibole precipitation has been inferred through distinctive geochemical fingerprints of derivative products, this study provides a direct snapshot of this differentiation process. With progressive accumulation, an amphibole-rich sponge will form in arc crust, which is fundamental to interpreting a wide range of issues in petrology (e.g., Davidson et al. 2007; Edmonds et al. 2019; Sparks et al. 2019) and perhaps for the genesis of ore-forming magmas (e.g., Hou et al. 2015b, 2017). In addition, the studied amphibole-rich xenoliths have petrological similarities to appinite, suggesting that some appinites may represent amphibole-rich cumulates. This has important implications for understanding the genesis of some unusual but petrologically significant rocks, such as high Ba–Sr granites and sanukitoids (Murphy 2013).

#### ACKNOWLEDGMENTS

We appreciate Chang-Ming Xing and Le Zhang for assistance on the electron microprobe and the LA-ICP-MS analyses, as well as Jun Wang for helpful discussions. We are grateful to Calvin Barnes, Emily Chin, and Associate Editor Christy Till for their very constructive, considerate, and detailed reviews that greatly improved this paper.

## FUNDING

This research was supported in part by the National Key Research and Development Program of China “Deep Structure and Ore-forming Process of Main Mineralization System in Tibetan Orogen” (2016YFC0600306) to Z.-S. Yang, the National Natural Science Foundation of China (91855215 and 41630208) and GIGCAS 135 project (135TP201601) to Q. Wang, the National Natural Science Foundation of China (41802061) to J.-S. Zhou.

## REFERENCES CITED

- Alonso-Perez, R., Müntener, O., and Ulmer, P. (2009) Igneous garnet and amphibole fractionation in the roots of island arcs: Experimental constraints on andesitic liquids. *Contributions to Mineralogy and Petrology*, 157, 541–558.
- Annen, C., Blundy, J.D., and Sparks, R.S.J. (2006) The genesis of intermediate and silicic magmas in deep crustal hot zones. *Journal of Petrology*, 47, 505–539.
- Arculus, R.J., and Wills, K.J.A. (1980) The petrology of plutonic blocks and Inclusions from the Lesser Antilles Island Arc. *Journal of Petrology*, 21, 743–799.
- Bachmann, O., and Huber, C. (2016) Silicic magma reservoirs in the Earth’s crust. *American Mineralogist*, 101, 2377–2404.
- (2019) The inner workings of crustal distillation columns; the physical mechanisms and rates controlling phase separation in silicic magma reservoirs. *Journal of Petrology*, 60, 3–18.
- Bachmann, O., Miller, C.F., and de Silva, S.L. (2007) The volcanic-plutonic connection as a stage for understanding crustal magmatism. *Journal of Volcanology and Geothermal Research*, 167, 1–23.
- Barnes, C.G., Coint, N., and Yoshinobu, A. (2016) Crystal accumulation in a tilted arc batholith. *American Mineralogist*, 101, 1719–1734.
- Barnes, C.G., Berry, R., Barnes, M.A., and Ernst, W.G. (2017) Trace element zoning in hornblende: Tracking and modeling the crystallization of a calc-alkaline arc pluton. *American Mineralogist*, 102, 2390–2405.
- Bloomer, S.H., Stern, R.J., Fisk, E., and Geschwind, C.H. (1989) Shoshonitic volcanism in the Northern Mariana Arc: 1. Mineralogic and major and trace element characteristics. *Journal of Geophysical Research: Solid Earth*, 94, 4469–4496.
- Blundy, J., and Wood, B. (1994) Prediction of crystal-melt partition coefficients from elastic moduli. *Nature*, 372, 452–454.
- Brice, J.C. (1975) Some thermodynamic aspects of the growth of strained crystals. *Journal of Crystal Growth*, 28, 249–253.
- Brown, M. (2013) Granite: From genesis to emplacement. *GSA Bulletin* 125, 1079–1113.
- Cashman, K.V., Sparks, R.S.J., and Blundy, J.D. (2017) Vertically extensive and unstable magmatic systems: A unified view of igneous processes. *Science*, 355, eaag3055.
- Chang, J., and Audétat, A. (2018) Petrogenesis and metal content of hornblende-rich xenoliths from two Laramide-age magma systems in southwestern USA: insights into the metal budget of arc magmas. *Journal of Petrology*, 59, 1869–1898.
- Chappell, B.W., and White, A.J.R. (1992) I- and S-type granites in the Lachlan fold belt. *Transactions of the Royal Society of Edinburgh, Earth Science*, 83, 1–26.
- Chin, E.J. (2018) Deep crustal cumulates reflect patterns of continental rift volcanism beneath Tanzania. *Contributions to Mineralogy and Petrology*, 173, 85.
- Chin, E.J., Shimizu, K., Bybee, G.M., and Erdman, M.E. (2018) On the development of the calc-alkaline and tholeiitic magma series: A deep crustal cumulate perspective. *Earth and Planetary Science Letters*, 482, 277–287.
- Chung, S.L., Chu, M.F., Zhang, Y., Xie, Y., Lo, C.H., and Lee, T.Y. (2005) Tibetan tectonic evolution inferred from spatial and temporal variations in post-collisional magmatism. *Earth-Science Reviews*, 68, 173–196.
- Clemens, J.D., and Stevens, G. (2012) What controls chemical variation in granitic magmas? *Lithos*, 134, 317–329.
- Coleman, D.S., Bartley, J.M., Glazner, A.F., and Pardue, M.J. (2012) Is chemical zonation in plutonic rocks driven by changes in source magma composition or shallow-crustal differentiation? *Geosphere*, 8, 1568–1587.
- Compton, R.R. (1958) Significance of amphibole paragenesis in the Bidwell Bar region, California. *American Mineralogist*, 43, 890–907.
- Cooper, G.F., Davidson, J.P., and Blundy, J.D. (2016) Plutonic xenoliths from Martinique, Lesser Antilles: evidence for open system processes and reactive melt flow in island arc crust. *Contributions to Mineralogy and Petrology*, 171, 87.
- Davidson, J., and Wilson, M. (2011) Differentiation and source processes at Mt Pelee and the Quill; active volcanoes in the Lesser Antilles Arc. *Journal of Petrology*, 52, 1493–1531.
- Davidson, J., Turner, S., Handley, H., Macpherson, C., and Dossato, A. (2007) Amphibole “sponge” in an arc crust? *Geology*, 35, 787–790.
- Davidson, J., Turner, S., and Plank, T. (2013) Dy/Dy\*: variations arising from mantle sources and petrogenetic processes. *Journal of Petrology*, 54, 525–537.
- Ding, L., Maksatbek, S., Cai, F., Wang, H., Song, P., Ji, W., Xu, Q., Zhang, L., and Upendra, B. (2017) Processes of initial collision and suturing between India and Asia. *Science China Earth Sciences*, 60, 635–651.
- Edmonds, M., Cashman, K.V., Holness, M., and Jackson, M. (2019) Architecture and dynamics of magma reservoirs. *Philosophical Transactions of the Royal Society of London A: Mathematical, Physical and Engineering Sciences*, 377, 20180298.
- Erdmann, S., Martel, C., Pichavant, M., and Kushnir, A. (2014) Amphibole as an archivist of magmatic crystallization conditions: problems, potential, and implications for inferring magma storage prior to the paroxysmal 2010 eruption of Mount Merapi, Indonesia. *Contributions to Mineralogy and Petrology*, 167, 1016.
- Ghiorso, M.S. (1997) Thermodynamic models of igneous processes. *Annual Review of Earth and Planetary Sciences*, 25, 221–241.
- Ghiorso, M.S., and Sack, R.O. (1995) Chemical mass-transfer in magmatic processes. 4. A revised and internally consistent thermodynamic model for the interpolation and extrapolation of liquid-solid equilibria in magmatic systems at elevated temperatures and pressures. *Contributions to Mineralogy and Petrology*, 119, 197–212.
- Glazner, A., Coleman, D., and Mills, R. (2015) *The Volcanic-Plutonic Connection*, 1–22. Springer.
- Grove, T.L., and Brown, S.M. (2018) Magmatic processes leading to compositional diversity in igneous rocks: Bowen (1928) revisited. *American Journal of Science*, 318, 1–28.
- Grove, T.L., Parman, S.W., Bowring, S.A., Price, R.C., and Baker, M.B. (2002) The role of an H<sub>2</sub>O-rich fluid component in the generation of primitive basaltic andesites and andesites from the Mt. Shasta region, N California. *Contributions to Mineralogy and Petrology*, 142, 375–396.
- Grove, T.L., Elkins-Tanton, L.T., Parman, S.W., Chatterjee, N., Müntener, O., and Gaetani, G.A. (2003) Fractional crystallization and mantle-melting controls on calc-alkaline differentiation trends. *Contributions to Mineralogy and Petrology*, 145, 515–533.
- Hawkesworth, C.J., Gallagher, K., Hergt, J.M., and McDermott, F. (1993) Mantle and slab contributions in arc magmas. *Annual Review of Earth and Planetary Sciences*, 21, 175–204.
- Hildreth, W., and Moorbath, S. (1988) Crustal contributions to arc magmatism in the Andes of Central Chile. *Contributions to Mineralogy and Petrology*, 98, 455–489.
- Humphreys, M.C.S., Zhang, J., Cooper, G.F., Macpherson, C.G., and Ottley, C.J. (2019a) Identifying the ingredients of hydrous arc magmas: insights from Mt Lamington, Papua New Guinea. *Philosophical Transactions of the Royal Society A*, 377, 20180018.
- Humphreys, M.C., Cooper, G.F., Zhang, J., Loewen, M., Kent, A.J., Macpherson, C.G., and Davidson, J.P. (2019b) Unravelling the complexity of magma plumbing at Mount St. Helens: a new trace element partitioning scheme for amphibole. *Contributions to Mineralogy and Petrology*, 174, 9.
- Hou, K.J., Li, Y.H., and Tian, Y.Y. (2009) In situ U–Pb zircon dating using Laser Ablation Multi Ion Counting-ICP-MS. *Mineral Deposits*, 28, 481–492 (in Chinese with English abstract).
- Hou, Z., Li, Q., Gao, Y., Lu, Y., Yang, Z., Wang, R., and Shen, Z. (2015b) Lower-Crustal magmatic hornblende in North China Craton: insight into the genesis of porphyry Cu deposits. *Economic Geology*, 110, 1879–1904.
- Hou, Z., Duan, L., Lu, Y., Zheng, Y., Zhu, D., Yang, Z., Yang, Z., Wang, B., Pei, Y., Zhao, Z., and McCuaig, C. (2015a) Lithospheric architecture of the Lhasa terrane and its control on ore deposits in the Himalayan-Tibetan orogen. *Economic Geology*, 110, 1541–1575.
- Hou, Z., Zhou, Y., Wang, R., Zheng, Y., He, W., Zhao, M., Evans, N.J., Weinberg, R.F. (2017) Recycling of metal-fertilized lower continental crust: Origin of non-arc Au-rich porphyry deposits at cratonic edges. *Geology*, 45, 563–566.
- Jagoutz, O.E. (2010) Construction of the granulitoid crust of an island arc. Part II: a quantitative petrogenetic model. *Contributions to Mineralogy and Petrology*, 160, 359–381.
- Jagoutz, O., and Klein, B. (2018) On the importance of crystallization-differentiation for the generation of SiO<sub>2</sub>-rich melts and the compositional build-up of arc (and continental) crust. *American Journal of Science*, 318, 29–63.
- Jagoutz, O., Müntener, O., Burg, J.-P., Ulmer, P., and Jagoutz, E. (2006) Lower continental crust formation through focused flow in km-scale melt conduits: The zoned ultramafic bodies of the Chilas Complex in the Kohistan arc (NW Pakistan). *Earth and Planetary Science Letters*, 320, 320–342.
- Ji, W.-Q., Wu, F.-Y., Chung, S.-L., Li, J.-X., and Liu, C.-Z. (2009) Zircon U–Pb geochronology and Hf isotopic constraints on petrogenesis of the Gangdese batholith, southern Tibet. *Chemical Geology*, 262, 229–245.
- Ji, W.-Q., Wu, F.-Y., Chung, S.-L., and Liu, C.-Z. (2014) The Gangdese magmatic constraints on a latest Cretaceous lithospheric delamination of the Lhasa terrane, southern Tibet. *Lithos*, 210, 168–180.
- Klaver, M., Matveev, S., Berndt, J., Lissenberg, C.J., and Vroon, P.Z. (2017) A mineral and cumulate perspective to magma differentiation at Nisyros volcano, Aegean arc. *Contributions to Mineralogy and Petrology*, 172, 95.
- Krawczynski, M.J., Grove, T.L., and Behrens, H. (2012) Amphibole stability in primitive arc magmas: effects of temperature, H<sub>2</sub>O content, and oxygen fugacity. *Contributions to Mineralogy and Petrology*, 164, 317–339.
- Leake, B., Woolley, A., Arps, C., Birch, W., Gilbert, M., Grice, J., Hawthorne, F., Kato, A., Kisch, H., Krivovichev, V., and others. (1997) Nomenclature of amphiboles: Report of the Subcommittee on Amphiboles of the International Mineralogical Association, Commission on New Minerals and Mineral Names. *American Mineralogist*, 82, 1019–1037.
- Lee, C.T.A., and Bachmann, O. (2014) How important is the role of crystal fractionation in making intermediate magmas? Insights from Zr and P systematics. *Earth and Planetary Science Letters*, 393, 266–274.
- Liu, Y., Gao, S., Hu, Z., Gao, C., Zong, K., and Wang, D. (2010) Continental and

- oceanic crust recycling-induced melt-peridotite interactions in the Trans-North China Orogen: U–Pb dating, Hf isotopes and trace elements in zircons of mantle xenoliths. *Journal of Petrology*, 51, 537–571.
- Ma, L., Wang, Q., Li, Z.-X., Wyman, D.A., Jiang, Z.-Q., Yang, J.-H., Gou, G.-N., and Guo, H.-F. (2013) Early late Cretaceous (ca. 93 Ma) norites and hornblendites in the Milin area eastern Gangdese: Lithosphere–asthenosphere interaction during slab roll-back and an insight into early late Cretaceous (ca. 100–80 Ma) magmatic “flare-up” in southern Lhasa (Tibet). *Lithos*, 172, 17–30.
- Ma, L., Wang, Q., Kerr, A.C., Yang, J.-H., Xia, X.-P., Quan, O., Yang, Z.-Y., and Sun, P. (2018) Paleocene (c. 62 Ma) Leucogranites in Southern Lhasa, Tibet: products of syn-collisional crustal anatexis during slab roll-back? *Journal of Petrology*, 58, 2089–2114.
- Ma, X., Meert, J.G., Xu, Z., and Yi, Z. (2018) Late Triassic intra-oceanic arc system within Neotethys: Evidence from cumulate appinites in the Gangdese belt, southern Tibet. *Lithosphere*, 10, 545–565.
- Martin, R.F. (2007) Amphiboles in the igneous environment. *Reviews in Mineralogy and Geochemistry*, 67, 323–358.
- Melekhova, E., Blundy, J., Martin, R., Arculus, R., and Pichavant, M. (2017) Petrological and experimental evidence for differentiation of water-rich magmas beneath St. Kitts, Lesser Antilles. *Contributions to Mineralogy and Petrology*, 172, 98.
- Meng, Y., Xu, Z., Santosh, M., Ma, X., Chen, X., Guo, G., and Liu, F. (2016) Late Triassic crustal growth in southern Tibet: evidence from the Gangdese magmatic belt. *Gondwana Research*, 37, 449–464.
- Meurer, W.P., and Boudreau, A.E. (1998) Compaction of igneous cumulates Part I: Geochemical consequences for cumulates and liquid fractionation trends. *The Journal of Geology*, 106, 281–292.
- Mo, X., Niu, Y., Dong, G., Zhao, Z., Hou, Z., Zhou, S., and Ke, S. (2008) Contribution of syncollisional felsic magmatism to continental crust growth: a case study of the Paleogene Linzizong volcanic succession in southern Tibet. *Chemical Geology*, 250, 49–67.
- Müntener, O., and Ulmer, P. (2018) Arc crust formation and differentiation constrained by experimental petrology. *American Journal of Science*, 318, 64–89.
- Murphy, J.B. (2013) Appinitic suites: a record of the role of water in the genesis, transport, emplacement and crystallization of magma. *Earth-Science Reviews*, 119, 35–59.
- O'Neill, H.St.C., and Pownceby, M.I. (1993) Thermodynamic data from redox reactions at high temperatures. I. An experimental and theoretical assessment of the electrochemical method using stabilized zirconia electrolytes, with revised values for the Fe–FeO, Co–CoO, Ni–NiO and Cu–Cu<sub>2</sub>O oxygen buffers, and new data for the W–WO<sub>2</sub> buffer. *Contributions to Mineralogy and Petrology*, 114, 296–314.
- Othman, D.B., White, W.M., and Patchett, J. (1989) The geochemistry of marine sediments, island arc magma genesis, and crust–mantle recycling. *Earth and Planetary Science Letters*, 94, 1–21.
- Petford, N., Cruden, A.R., McCaffrey, K.J.W., and Vigneresse, J.L. (2000) Granite magma formation, transport and emplacement in the Earth's crust. *Nature*, 408, 669–673.
- Plank, T., and Langmuir, C.H. (1993) Tracing trace elements from sediment input to volcanic output at subduction zones. *Nature*, 362, 739–743.
- Plank, T., Kelley, K.A., Zimmer, M.M., Hauri, E.H., and Wallace, P.J. (2013) Why do mafic arc magmas contain ~4 wt% water on average? *Earth and Planetary Science Letters*, 364, 168–179.
- Putirka, K.D. (2016) Amphibole thermometers and barometers for igneous systems and some implications for eruption mechanisms of felsic magmas at arc volcanoes. *American Mineralogist*, 101, 841–858.
- Putirka, K.D., Canchola, J., Rash, J., Smith, O., Torrez, G., Paterson, S.R., and Ducea, M.N. (2014) Pluton assembly and the genesis of granitic magmas: Insights from the GIC pluton in cross section, Sierra Nevada Batholith, California. *American Mineralogist*, 99, 1284–1303.
- Ridolfi, F., Renzulli, A., and Puerini, M. (2010) Stability and chemical equilibrium of amphibole in calc-alkaline magmas: an overview, new thermobarometric formulations and application to subduction-related volcanoes. *Contributions to Mineralogy and Petrology*, 160, 45–66.
- Rudnick, R.L. (1995) Making continental crust. *Nature*, 378, 571–578.
- Rutherford, M.J., and Devine, J.D. (1988) The May 18, 1980, eruption of Mount St. Helens: 3. Stability and chemistry of amphibole in the magma chamber. *Journal of Geophysical Research: Solid Earth*, 93, 11949–11959.
- Sadofsky, S.J., Portnyagin, M., Hoernle, K., and van den Bogaard, P. (2008) Subduction cycling of volatiles and trace elements through the Central American volcanic arc: evidence from melt inclusions. *Contributions to Mineralogy and Petrology*, 155, 433–456.
- Shannon, R.D. (1976) Revised effective ionic radii and systematic studies of interatomic distances in halides and chalcogenides. *Acta Crystallographica*, A32, 751–767.
- Shimizu, K., Liang, Y., Sun, C., Jackson, C.R., and Saal, A.E. (2017) Parameterized lattice strain models for REE partitioning between amphibole and silicate melt. *American Mineralogist*, 102, 2254–2267.
- Smith, D.J. (2014) Clinopyroxene precursors to amphibole sponge in arc crust. *Nature Communications*, 5, 4329.
- Sparks, R.S.J., Annen, C., Blundy, J.D., Cashman, K.V., Rust, A.C., and Jackson, M.D. (2019) Formation and dynamics of magma reservoirs. *Philosophical Transactions of the Royal Society of London A: Mathematical, Physical and Engineering Sciences*, 377, 20180019.
- Stamper, C., Blundy, J., Arculus, R., and Melekhova, E. (2014) Petrology of plutonic xenoliths and volcanic rocks from Grenada, Lesser Antilles. *Journal of Petrology*, 55, 1353–1387.
- Stern, R.J., Bloomer, S.H., Lin, P.N., Ito, E., and Morris, J. (1988) Shoshonitic magmas in nascent arcs: New evidence from submarine volcanoes in the northern Marianas. *Geology*, 16(5), 426–430.
- Sun, S.-S., and McDonough, W.F. (1989) Chemical and isotopic systematics of oceanic basalts: implications for mantle composition and processes. *Geological Society, London, Special Publications*, 42, 313–345.
- Tatsumi, Y. (1989) Migration of fluid phases and genesis of basalt magmas in subduction zones. *Journal of Geophysical Research: Solid Earth*, 94, 4697–4707.
- Tiepolo, M., and Tribuzio, R. (2008) Petrology and U–Pb zircon geochronology of amphibole-rich cumulates with sanukitic affinity from Husky Ridge (Northern Victoria Land, Antarctica): insights into the role of amphibole in the petrogenesis of subduction-related magmas. *Journal of Petrology*, 49, 937–970.
- Tiepolo, M., Oberti, R., Zanetti, A., Vannucci, R., and Foley, S.F. (2007) Trace element partitioning between amphibole and silicate melt. *Reviews in Mineralogy and Geochemistry*, 67, 417–452.
- Tollan, P.M.E., Bindeman, I., and Blundy, J.D. (2012) Cumulate xenoliths from St. Vincent, Lesser Antilles island arc: a window into upper crustal differentiation of mantle-derived basalts. *Contributions to Mineralogy and Petrology*, 163, 189–208.
- Turner, S., Arnaud, N., Liu, J., Rogers, N., Hawkesworth, C., Harris, N., Kelley, S., van Calsteren, P., and Deng, W. (1996) Post-collision, shoshonitic volcanism on the Tibetan Plateau: Implications for convective thinning of the lithosphere and the source of Ocean Island Basalts. *Journal of Petrology*, 37, 45–71.
- Ulmer, P., and Trommsdorff, V. (1995) Serpentine stability to mantle depths and subduction-related magmatism. *Science*, 268, 858–861.
- Wang, J., Wang, Q., Dan, W., Yang, J.-H., Yang, Z.-Y., Sun, P., Qi, Y., and Hu, W.-L. (2019) The role of clinopyroxene in amphibole fractionation of arc magmas: Evidence from mafic intrusive rocks within the Gangdese arc, southern Tibet. *Lithos*, 338, 174–188.
- Wood, B.J., and Blundy, J.D. (1997) A predictive model for rare earth element partitioning between clinopyroxene and anhydrous silicate melt. *Contributions to Mineralogy and Petrology*, 129, 166–181.
- Xu, W.-C., Zhang, H.-F., Luo, B.-J., Guo, L., and Yang, H. (2015) Adakite-like geochemical signature produced by amphibole-dominated fractionation of arc magmas: an example from the Late Cretaceous magmatism in Gangdese belt, south Tibet. *Lithos*, 232, 197–210.
- Xu, W., Zhu, D.-C., Wang, Q., Weinberg, R.F., Wang, R., Li, S.-M., Zhang, L.-L., and Zhao, Z.-D. (2019) Constructing the Early Mesozoic Gangdese crust in southern Tibet by hornblende-dominated magmatic differentiation. *Journal of Petrology*, 60, 515–552.
- Zhang, J., Davidson, J.P., Humphreys, M.C.S., Macpherson, C.G., and Neill, I. (2015) Magmatic enclaves and andesitic lavas from Mt. Lamington, Papua New Guinea: implications for recycling of earlier-fractionated minerals through magma recharge. *Journal of Petrology*, 56, 2223–2256.
- Zhang, J., Humphreys, M.C.S., Cooper, G.F., Davidson, J.P., and Macpherson, C.G. (2017) Magma mush chemistry at subduction zones, revealed by new melt major element inversion from calcic amphiboles. *American Mineralogist*, 102, 1353–1367.
- Zhang, L., Ren, Z.-Y., Xia, X.-P., Yang, Q., Hong, L.-B., and Wu, D. (2019) In situ determination of trace elements in melt inclusions using laser ablation inductively coupled plasma sector field mass spectrometry. *Rapid Communications in Mass Spectrometry*, 33, 361–370.
- Zhu, D.-C., Zhao, Z.-D., Niu, Y., Mo, X.-X., Chung, S.-L., Hou, Z.-Q., Wang, L.-Q., and Wu, F.-Y. (2011) The Lhasa Terrane: record of a microcontinent and its histories of drift and growth. *Earth and Planetary Science Letters*, 301, 241–255.

MANUSCRIPT RECEIVED JULY 9, 2019

MANUSCRIPT ACCEPTED OCTOBER 3, 2019

MANUSCRIPT HANDLED BY CHRISTY TILL

## Endnote:

<sup>1</sup>Deposit item AM-20-27199, Supplemental Figures and Tables. Deposit items are free to all readers and found on the MSA website, via the specific issue's Table of Contents (go to [http://www.minsocam.org/MSA/AmMin/TOC/2020/Feb2020\\_data/Feb2020\\_data.html](http://www.minsocam.org/MSA/AmMin/TOC/2020/Feb2020_data/Feb2020_data.html)).